Journal of Materials Chemistry B

ROYAL SOCIETY OF CHEMISTRY

PAPER

View Article Online
View Journal | View Issue

Check for updates

Cite this: J. Mater. Chem. B, 2023, 11, 2166

A mace-like heterostructural enriched injectable hydrogel composite for on-demand promotion of diabetic wound healing†

Li Wang, [ab] Zahid Hussain, [ab] Penghui Zheng,[b] Yajie Zhang, [b] Yi Cao, [b] Tong Gao,[b] Zhuangzhuang Zhang,[ab] Yuehu Zhang[b] and Renjun Pei*[ab]

Received 3rd November 2022,
Accepted 24th January 2023

DOI: 10.1039/d2tb02403a

rsc.li/materials-b

Wound healing is a multifaceted process that involves hemostasis, inflammation, proliferation, and remodeling stages. Diabetic wounds affect the transition of the organized phases and result in delayed healing due to impaired angiogenesis, chronic inflammation, bacterial infection, and insufficient growth factors. Multifunctional heterostructural nanoparticles enriched minimally invasive hydrogels for on-demand procedural distribution to aid wound healing at various stages has become a promising strategy. Herein, silk fibroin-hyaluronic acid based injectable hydrogels incorporated with mace-like Au–CuS heterostructural nanoparticles (gAu–CuS HSs) were used to cure diabetic wounds. SF–HA and the rough surface of gAu–CuS HSs confer a synergistic hemostatic phase with a nano-bridge effect and rapidly close the wounds. During the inflammation stage, gAu–CuS HSs perform in-space resonance energy transfer under 808 nm laser irradiation which in return produces reactive oxygen species for bacterial destruction. The unusual mace-like rough structure of nanoparticles causes macrophage transfer to the M2 phenotype, regulates cytokine expression (interleukin 6, transforming factor-β1, interferon γ, and interleukin-10), promotes angiogenesis, and promotes cell multiplication and fibroblast emigration to the wound area during the proliferation and remodeling phase. Overall, the gAu–CuS HSs reinforced injectable hydrogel programmatically accelerates wound healing and could represent a versatile strategy for advanced diabetic wound healing.

Open Access Article. Published on 25 2023. Downloaded on 30.5.2026 16:35:55.
This article is licensed under a Creative Commons Attribution-NonCommercial 3.0 Unported Licence.

1. Introduction

Diabetes is a frequent chronic metabolic condition defined by sustained hyperglycemia with long-term health effects.[1] The poor healing of diabetic wounds is predicted to impact 25% of all diabetes mellitus patients.[2] Diabetic wounds are more susceptible to bacterial infection and have difficulty healing themselves due to impaired defence mechanisms, impaired angiogenesis, chronic inflammation, and insufficient secretion of growth factors. The delayed healing of the wound contributed to increased healthcare costs, morbidity, and mortality.[3] Therefore, there is an imperative need to address impaired wound healing problems for diabetic patients.

Wound healing is a complex and multifaceted biological procedure involving hemostasis, inflammation, proliferation, and remodeling stages. The rapid occurrence of hemostasis can prevent blood loss and promote immediate wound closure.[4–6] The inhibition of bacterial infection can accelerate the transition to the inflammatory stage and facilitate wound healing. Subsequently cell proliferation, cell migration, and the creation of new blood vessels that occurs at the proliferative wound phase are critical for wound healing.[7,8] For instance, during adult wound healing, the local pro-inflammatory macrophage phenotype (M1) transforms into anti-inflammatory macrophages (M2) based on spatiotemporal signals and is crucial for cell proliferation, angiogenesis, vascularization, and collagen deposition.[9–13] The synchronization of numerous stages is necessary for wound healing; however, the biological environment inherent in diabetes results in delayed wound healing and disrupts the transition between orderly phases.[14,15]

Recently, various metal-based antibacterial, semiconductor, and rough surface nanomaterials, including metal and carbon nanomaterials (Ag,[16] Au,[17] CuO, ZnO,[18] and graphene), have gained attention as a potential material to promote wound healing. Metal-based nanoparticles with high surface roughness can exhibit a nanobridge effect which could facilitate the adhesion of wounded skins, and can prevent blood/fluid losses.[19–21]

[a] School of Nano-Tech and Nano-Bionics, University of Science and Technology of China, Hefei, 230026, China. E-mail: rjpei2011@sinano.ac.cn
[b] CAS Key Laboratory for Nano-Bio Interface, Suzhou Institute of Nano-Tech and Nano-Bionics, Chinese Academy of Sciences, Suzhou, 215123, China

† Electronic supplementary information (ESI) available. See DOI: https://doi.org/10.1039/d2tb02403a

This journal is © The Royal Society of Chemistry 2023

Open Access Article. Published on 25 2023. Downloaded on 30.5.2026 16:35:55.
This article is licensed under a Creative Commons Attribution-NonCommercial 3.0 Unported Licence.

Although the mechanism underlying this nanobridge effect remains unclear, the surface architecture of nanoparticles could play a crucial role in encouraging hemostasis.[22–24] In the inflammatory stage, metal–semiconductor nanomaterials with active electronic properties can generate energetic charge carriers (electrons and holes) after exposure to suitable light to form reactive oxygen species (ROS), which can efficiently kill pathogenic bacterial species. It could act as a substitute for antibiotics to tackle antimicrobial-resistant problems and advance the inflammation stage of healing.[25–27] However, their accessibility in actual application suffered from intractable limitations, *e.g.*, due to the substantial band gaps of these nanomaterials, only UV light can be employed to excite the charge carriers (electrons and holes), but at the cost of pain and underlying skin damage[10,26,28,29] Furthermore, electron–hole recombination limits the ROS production capacity, which results in inadequate bacterial killing. Therefore, the development of nanoparticles capable of generating ROS after mild near-infrared light (NIR) exposure and facilitating electron–hole separation could be more promising for the inflammatory stage of wound healing.[30–32] Recent research found that nanoparticles with rough surface texture accelerate the proliferation (polarizing macrophages to the anti-inflammatory M2 state) and remodeling phases (promoting collagen deposition) of wound healing.[33,34] However, these studies are based on flat models unsuitable for their biomedical applications.[35] Therefore, rough surface textured metal heterostructures can regulate macrophage M2 polarization and promote multistage wound healing in multiple stages.

Hydrogels are commonly used as promising scaffolds for wound dressings,[36] because they offer numerous attractive properties such as 3D microporosity, soft consistency,[37] exudation absorption potential, freezing wounds, and material-dependent bio-adhesiveness. They can be formed *via* chemical, enzymatic, thermal, or light-induced crosslinking between polymeric chains of molecules. Hydrogels provide a 3D microstructural framework for cell encapsulation, cell migration, drug delivery (antibiotics, inorganic nanoparticles, antioxidants, growth factors), and tissue regeneration.[38–40] The injectable hydrogel has been recognized as an artificial extracellular matrix, and could better cover irregular-shaped wounds than a simple photopolymerizable hydrogel scaffold. It could be more suitable for tissue engineering because of the elimination of surgical implantation.[41,42] It is difficult to speed up wound healing in diabetic patients due to the involvement of multiple factors, including large wound areas, severe bacterial infection, *etc.*, and therefore, the development of multifunctional hydrogels (hemostatic, antibacterial, pro-angiogenic, anti-inflammatory, and pro-regenerative) is particularly desirable for clinical applications. The multifunctional heterostructural nanoparticle enriched minimally invasive injectable hydrogel system for on-demand procedural distribution to aid wound healing at various stages has become a promising strategy with less concern for antibiotic resistance.

Herein, novel mace-like Au–CuS heterostructures (gAu–CuS HSs) are synthesized and incorporated in silk fibroin (SF)–hyaluronic acid (HA) based injectable hydrogels for the multistage programmed acceleration of wound healing (Fig. 1). The composite of natural HA and SF combines useful properties of both constituents and exhibits a better control of gelation time and mechanical performance. Furthermore, the application of an enzyme-dependent cross-linking process [horseradish peroxidase (HRP) and hydrogen oxide (H_2O_2)] could tune the biophysical properties and increase the applicability of scaffolds to different wound conditions. Our study highlighted that adding mace-like Au–CuS hetero-structures could impart stable rheological properties, and their synergistic combination with an injectable hydrogel could form a nanobridge and seal the large diabetic wound, thereby realizing the programmed acceleration of the hemostasis stage. The gAu–CuS HSs hydrogel can generate a substantial amount of ROS under NIR illumination. Under the excitation of incident light, the Au–CuS heterostructure experiences localized surface plasmon resonance (LSPR), which encourages the formation of high-energy carriers. The mace-like Au–CuS heterostructure can promote the spatial separation of charge carriers arranged at the Fermi level on different metals, resulting in more remarkable photodynamic performance. During the inflammatory stage, a large amount of ROS produced by the gAu–CuS HSs hydrogel induced anti-bacterial activity. At the proliferation and remodeling stage, a rough-textured mace-like structure can increase the macrophage polarization towards the M2 phenotype, showing increased interleukin-10 (IL-10) plus transforming factor-β1 (TGF-β1) expression, promoting angiogenesis and collagen production in wounds. This study breaks the singleness of materials for wound treatment and provides new insight into programmed wound healing acceleration by integrating an injectable bioactive hydrogel, nanomaterials' nano topology, and plasmonic performance.

2. Materials and methods

2.1. Chemicals and reagents

Cetyltrimethylammonium bromide (CTAB, ≥98.0%), silver nitrate ($AgNO_3$, ≥99%), sodium borohydride ($NaBH_4$, 98%), hydroquinone (HQ, ≥9%), anhydrous copper chloride ($CuCl_2$, 99.9%), lithium bromide (LiBr, 99.9%), gold(III) chloride trihydrate ($HAuCl_4{\cdot}3H_2O$, 98%), and potassium tetrachloroplatinate(II) (K_2PtCl_4) were purchased from Sigma-Aldrich. Fetal bovine serum (FBS, Gibco), Trypsin-EDTA (Hyclone), penicillin-streptomycin (Merck Millipore, USA), Dulbecco's modified Eagle's medium (DMEM, Gibco), and deionized water (DI; resistivity, 18.2 MΩ cm) were used in different experiments.

2.2. Growth of the Au nanorods (NRs), Au–CuS HSs and Au–CuS CSs nanostructures

Au NRs were prepared in an aqueous solution using a seed-mediated method. In brief, a total volume of 5 mL of $HAuCl_4{\cdot}3H_2O$ (0.5 mM) and CTAB (0.1 mM) was thoroughly mixed. Add 600 μL of $NaBH_4$ (0.01 M) to the above solution and rest for 0.5 h at 37 °C. To synthesize Au NR growth solution, 10 mL of

Open Access Article. Published on 25 2023. Downloaded on 30.5.2026 16:35:55.
This article is licensed under a Creative Commons Attribution-NonCommercial 3.0 Unported Licence.

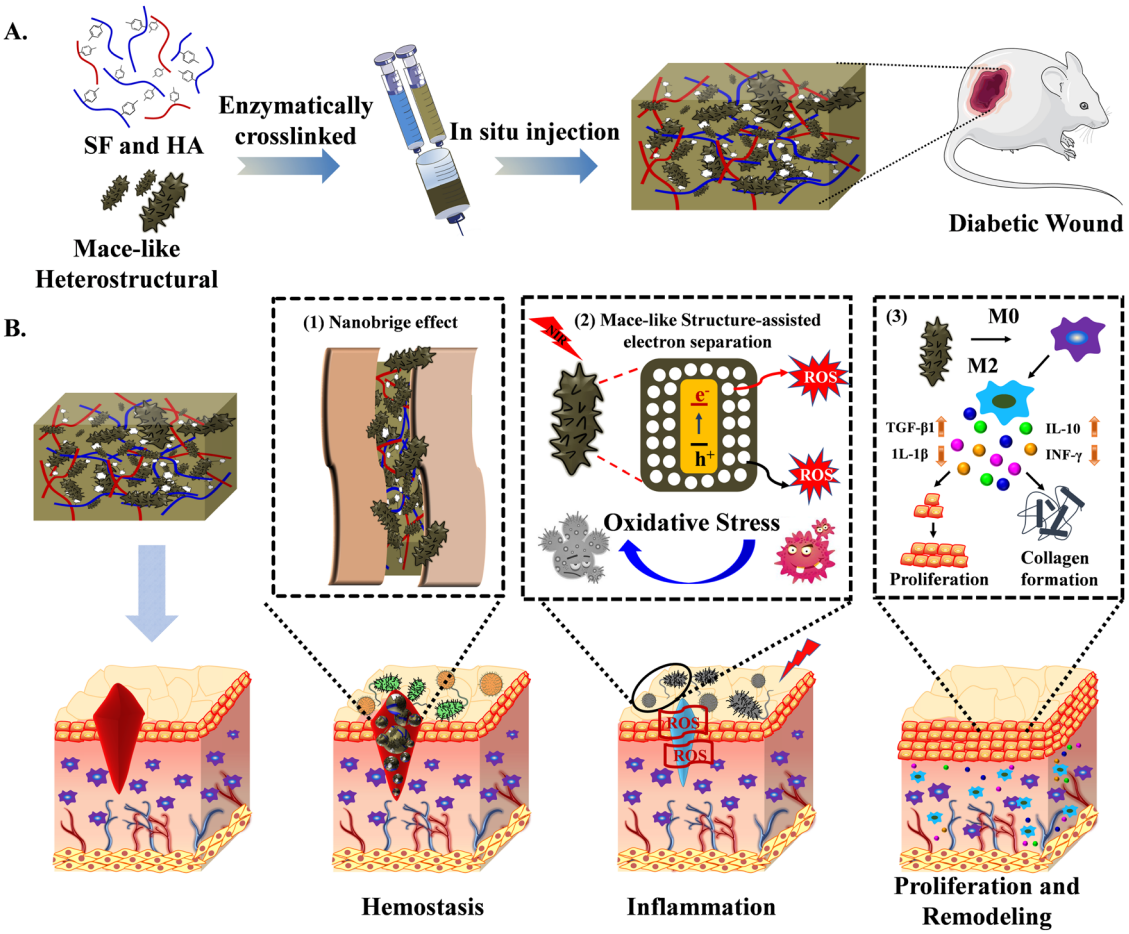

Fig. 1 Schematic diagram representation of gAu–CuS HSs hydrogel for treating diabetic wound healing. (A) Fabrication of SF–HA hydrogels incorporating Au–CuS HSs for injection at the wound site. (B) Schematic illustration of multiple stages of the wound healing process programmed by gAu–CuS HSs. (B_1) In the hemostasis stage, gAu–CuS HSs can act as nanobridges to seal wounds; (B_2) in the inflammatory phase, Au–CuS HSs with strong LSPR under near-infrared light excitation generate ROS to kill bacteria; (B_3) in the proliferation and remodeling stage, gAu–CuS HSs can facilitate the polarization of macrophages toward the M2 phenotype, regulate cytokines, promote cell proliferation, and tissue remodeling in the wounded area.

0.1 M CTAB was mixed with 1 mL of $HAuCl_4 \cdot 3H_2O$ (0.005 M). 0.12 mL of silver nitrate ($AgNO_3$, 0.1 M) solution was added, stirred well, and then 600 μL of hydroquinone (0.1 M) solution was added. This time, the reaction color changed from yellow to colorless. After vigorous stirring for 1 min, 0.075 mL of the Au seed solution (prepared above) were added and stirring was continued for 3 min, and rested for 12 h at 40 °C in the dark. Finally, centrifugation was used to collect Au NRs (8000 rpm for 10 min).

The synthesized Au NPs solution (5 mL) was collected and washed 3 times with water to remove excess surfactant. It was then redispersed into 5 mL of CTAB solution (1 mM). K_2PtCl_4 solution (5 mM, 200 μL) was then added to the Au NR solution with gentle shaking for 5 min to allow $PtCl4^{2-}$ to adsorb on the Au NR. The freshly prepared 500 μL $CuCl_2$ solution (0.5 M) and deionized water (4.3 mL) were then added to the Au NR solution sequentially. The final total volume of the solution was 10 mL. It was then put in the oven at 100 °C for 60 min to obtain Au–CuS HSs with a rough surface texture. Similar steps to this were used to synthesize Au–CuS CSs. The difference is that K_2PtCl_4 solution (1 mM, 200 μL) and $CuCl_2$ solution (0.1 mM, 500 μL) were used.

2.3. Synthesis of tyramine (Tyr) modified hyaluronic acid (HA)

Conjugating HA with Tyr was achieved through a reaction between the carboxylic groups of HA and the amine groups of Tyr. In brief, 2 g of sodium hyaluronate (M_w = 34 kDa) were dissolved in 80 mL of 2-morpholinoethane sulfonic acid (MES, 100 mM) buffer, before adding 2.86 g 1-ethyl-3-(3-dimethylaminopropyl) carbodiimide (DEC) and 1.72 g *N*-hydroxy succinimide (NHS). The solution was stirred for 60 min at 25 °C to activate the carboxyl groups on the HA molecule. Subsequently, 1.72 g of Tyr was added to the above mixture, and the pH was amended to about 8 with sodium hydroxide (NaOH) solution. The reaction mixture was stirred overnight at 25 °C under light-proof conditions. After the incubation reaction, the reactants were put in a dialysis bag (3.5 kDa) and dialyzed in sodium chloride (NaCl, 100 mM) buffer for 2 d, 25% alcohol solution for 2 d, and finally dialyzed in DI water for 2 d. After freeze-drying (for 3 d), HA–Tyr material was obtained

 This journal is © The Royal Society of Chemistry 2023

Open Access Article. Published on 25 2023. Downloaded on 30.5.2026 16:35:55.
This article is licensed under a Creative Commons Attribution-NonCommercial 3.0 Unported Licence.

as a fine-grained white powder and saved at 4 °C under dark conditions.

2.4. Fabrication of silk fibroin (SF) material

The cocoons (from *Bombyx mori*) were cut into thin slices, and their inner layer was removed. The peeled cocoons (10 g) were then boiled (at 95 °C) in 5 L 0.02 M sodium carbonate for 1 h to remove glue-like sericin (to prevent potential immunogenic host reactions) and to obtain degummed fibers. The obtained degummed fibers were cleaned with water to eliminate the greasy transparent material they carried and then dried at room temperature overnight. 5 g of degummed wire was dissolved in 25 mL 9.3 M LiBr solution and maintained at 65 °C for 240 min under continuous magnetic stirring. The mixture was diluted by a factor of 1.5 when the reaction was finished, and then it was put in a dialysis bag (MV 3.5 kDa). Finally, centrifugation was used to remove the insoluble silk particles (9000 rpm, 20 min) and then freeze-dried for two days. The SF material was then stored at 4 °C for future use.

2.5. Preparation of the SF–HA hydrogel and Au–CuS NP incorporated hydrogel

The total concentration of the SF and HA–Tyr polymer was 2% w/v. The SF/HA was combined in different ratios (0SF–100HA, 25SF–75HA, and 50SF–50HA) to form hydrogels. HRP and H_2O_2 concentrations were adjusted to different ratios to obtain the desired gelation rate and biophysical properties. The SF–HA hydrogel is formed using an enzymatic cross-linking reaction. Furthermore, SF–HA was mixed with varying concentrations of Au–CuS HSs and Au–CuS CSs, and then HRP and H_2O_2 were added for an enzymatic cross-linking reaction. The resultant nanomaterial incorporated hydrogel was named Au–CuS CSs hydrogels (gAu–CuS CSs hydrogels) and Au–CuS HSs hydrogels (gAu–CuS HSs hydrogels).

2.6. Characterization

The HA–Tyr conjugates were characterized using proton nuclear magnetic resonance spectroscopy (^{1}H-NMR, Varian NMR) using D_2O (δ = 4.65 ppm). The morphology and diameter of Au–CuS NPs were characterized by transmission electron microscopy (TEM, HT7700) operating at 50.0 kV. UV-Vis-NIR spectra were acquired using a UV-Vis spectrophotometer (UV-1280, Shimadzu). The zeta potential and hydrated particle size of Au–CuS NPs were analyzed by DLS (Zetasizer Nano, Malvern Instruments). X-ray diffraction (XRD, Rigaku-Dmax 2500) patterns were recorded using Cu Kα radiation with a step width of 10.0 deg min^{-1}. The specific surface area of nanoparticles was evaluated using the Brunauer–Emmett–Teller (BET) method. The nitrogen (N_2) adsorption–desorption isotherm was measured in an ASAP 2460 analyzer (Micromeritics, USA) at 120 °C for 12 h in a vacuum.

2.7. Production of ROS under near-infrared illumination

Total ROS produced by gAu–CuS was determined using 2′,7′-dichlorofluorescein (DCF) fluorescence. 80 μL of DCF working solution was added to each tube of the light-proof tube, then 20 μL PBS, Au–CuS HSs, Au–CuS CSs, SF–HA gel, gAu–CuS HSs or gAu–CuS CSs were added to each well (equivalent to 200 μg mL^{-1} Au–CuS). The mixture was subjected to an 808 nm near-infrared laser (0.75 W cm^{-2}, 10 min). After co-incubation for 6 h, excitation was performed using 490 nm, and DCF emission spectra were collected in the range of 500–600 nm.

2.8. Bacterial culture and antibacterial properties under near-infrared light irradiation

Escherichia coli (*E. coli*, Gram-negative) and *Staphylococcus aureus* (*S. aureus*, Gram-positive) were selected as typical bacterial strains for the antibacterial evaluation of our designed material. Bacterial strains were cultured by inoculating a single bacterial colony from a Luria-Bertani (LB) plate, then inoculated in 5 mL of Mueller Hinton Broth (MHB) medium and shaken at 150 rpm at 37 °C overnight. The estimated number of bacteria was identified by using the absorbance of the medium at 600 nm using a UV-Vis spectrophotometer. The bacterial solution was centrifuged, and the obtained bacterial pellet was resuspended and adjusted to 2×10^5 colony-forming units (CFU) mL^{-1} in PBS. Different concentrations of the gAu–CuS CSs hydrogel and gAu–CuS HSs hydrogel (equivalent to 200, 100, 50, and 25 μg mL^{-1} Au–CuS) were coated in 96-well plates. SF–HA gel without Au–CuS NPs was used as a control. After diluting the grown bacterial suspension to the absorbance level of 0.1 at 600 nm, add 150 μL (absorbance value = 0.1) bacterial suspension to each well. Then the laser was illuminated with 808 nm for 10 min with a power of 0.75 W cm^{-2}, and then move into a cell culture shaker (37 °C, 150 rpm) to continue the culture, monitor the absorption value at 600 nm every 1 h, and draw the bacterial growth curve.

At the same time, the antibacterial detection was carried out on an LB agar plate. In brief, 150 μL bacterial suspension was mixed with 50 μL of gAu–CuS CSs hydrogel or gAu–CuS HSs hydrogel (50 μg mL^{-1}) (equivalent to Au–CuS). After the laser was illuminated with 808 nm for 10 min with a power of 0.75 W cm^{-2}, it was placed in a bacterial culture shaker (37 °C, 150 rpm) for 30 min. The above bacterial culture suspension was serially diluted four-fold, aspirated 50 μL and laid on a solid agar medium. The cultured plate was placed for 37 °C growth for 24 h. Photographs were taken to record the antibacterial effect of the gAu–CuS CSs hydrogel and gAu–CuS HSs hydrogel on the bacterial CFU.

50 μL of gAu–CuS CSs hydrogel and gAu–CuS HSs hydrogel (50 μg mL^{-1}) (equivalent to Au–CuS) were gelatinized in a 48-well plate, and then 150 μL of bacterial culture solution was added to each group. After irradiating with an 808 nm laser for 10 min with a power of 0.75 W cm^{-2}, it was transferred to a bacterial culture shaker (37 °C, 150 rpm) for 6 h. Bacteria were gathered by centrifugation (3000 rpm for 5 min), washed 3 times with PBS, fixed with 2.5% glutaraldehyde (in 10× PBS) and dehydrated with ethanol gradient (30%, 50%, 75%, and 99%). Finally, the bacteria were dropped onto the silicon wafer and imaged under a SEM.

2.9. Detection of ROS, glutathione (GSH) content, and lipid peroxidation in bacteria

The production of ROS in bacteria was detected by staining bacteria with a 2′,7′-dichlorodihydrofluorescein diacetate

Open Access Article. Published on 25 2023. Downloaded on 30.5.2026 16:35:55.
This article is licensed under a Creative Commons Attribution-NonCommercial 3.0 Unported Licence.

(H_2DCF-DA) fluorescent probe. Briefly, 150 μL of bacterial suspension was mixed with 50 μL of gAu–CuS CSs hydrogel or gAu–CuS HSs hydrogel (50 μg mL^{-1}) (equivalent to Au–CuS). After irradiating with an 808 nm laser for 10 min with a power of 0.75 W cm^{-2}, it was transferred to a bacterial culture shaker (37 °C, 150 rpm) for 12 h. The bacterial s culture solution was then centrifuged, washed 4 times with PBS, and the obtained bacteria were stained with a H_2DCF-DA (10 μM) fluorescent probe for 30 min under dark conditions and studied under a confocal laser scanning microscope (CLSM, Olympus FV3000). The content of GSH in bacteria was measured using a 5,5′-dithiobis-(2-nitrobenzoic acid (DTNB)) method. Briefly, 150 μL bacterial suspension was mixed with 50 μL of gAu–CuS CSs hydrogel or gAu–HSs hydrogel (50 μg mL^{-1}) (equivalent to Au–CuS). Subsequently, the cells were irradiated with 808 nm laser light for 10 min with a power of 0.75 W cm^{-2} and then transferred to a bacterial culture shaker (37 °C, 150 rpm) for 12 h. The bacteria were washed 3 times with PBS and lysed well with 150 μL of lysis buffer (KeyGEN BioTECH). After centrifugation, 50 μL of supernatant was mixed with 100 μL of DTNB (30 μg mL^{-1}). The absorbance at 414 nm was detected after incubation for 30 min.

50 μL of gAu–CuS CSs hydrogel or gAu–CuS HSs hydrogel (50 μg mL^{-1}) (equivalent to Au–CuS) were gelatinized in a 48-well plate. Then 150 μL of the bacterial culture solution was added per well. After irradiating with an 808 nm (0.75 W cm^{-2}) laser for 10 min, the plate was transferred to a bacterial culture shaker (37 °C, 150 rpm) for 6 h. The bacteria were collected by centrifugation (3000 rpm for 10 min) and analyzed by MDA kit to calculate the degree of lipid peroxidation.

2.10. Cytocompatibility and hemocompatibility evaluation of the gAu–CuS CSs hydrogel and gAu–CuS HSs hydrogel

Mouse macrophages (RAW 264.7) and mouse embryonic fibroblasts (NIH 3T3) were cultured in DMEM. These cell lines were cultivated in a humidified (5% CO_2 at 37 °C) incubator until they reached ~80–85% confluency. The culture medium was renewed every 2 d. NIH 3T3 cells were sub-cultured by trypsinization, while RAW 264.7 cells were passaged by a cell scraper. The cells were counted (with a Neubauer chamber) and resuspended to obtain the desired concentration of cells for the next experiment. NIH 3T3 cells were seeded in 96-well plates at a cell density of 5×10^3 per well and incubated overnight. Afterwards, 100 μg mL^{-1} of gAu–CuS CSs hydrogel and gAu–CuS HSs hydrogel were added to the well plate and incubated for 24 h to 48 h. Finally, cell viability was quantified using the MTT assay according to the manufacturer instructions. At the same time, cells were stained with 20 μg mL^{-1} calcein and 20 μg mL^{-1} for 30 min. The samples were rinsed with PBS and studied under a CLSM to determine the live and dead cell ratio.

Hemolysis tests were performed using mouse red blood cell (RBCs) suspensions. Briefly, the pericardial blood of the mice was drawn by opening the abdominal cavity after anesthesia and placed in an EDTA vacuum blood collection tube. The blood was mixed and centrifuged (2000 rpm for 5 min) at 4 °C to pellet the RBCs. The purified RBCs (5%, v/v) were dispersed in PBS. Take the diluted RBC suspension (200 μL) and mix with the different components: (a) 1 mL ultrapure water as the positive control, (b) 1 mL PBS as the negative control, (c) 50 μL SF–HA hydrogel and 950 μL PBS, (d) 50 μL gAu–CuS CSs hydrogel and 950 μL PBS, (e) 50 μL of gAu–CuS HSs hydrogel and 950 μL of PBS, (f) 1 mL of Au–CuS CSs with variable concentrations (25, 50, 100, 200, and 400 μg mL^{-1}); (g) 1 mL Au–CuS HSs with variable concentrations (25, 50, 100, 200, and 400 μg mL^{-1}); the mixture was incubated in a CO_2 incubator at 37 °C for 2.5 h. The samples were taken out, the mixture was centrifuged at 2000 rpm for 10 min, and the hemolysis of erythrocytes after different treatments was recorded with a mobile camera. The supernatant was taken into a 96-well plate, and the absorbance of each sample (at 540 nm) was measured by a microplate reader. Hemolysis% for the different experimental groups was calculated using the following equation:

$$\text{Hemolysis (\%)} = [(A_h - A_n)/(A_w - A_n)] \times 100\%$$

where, A_h, A_n and A_w represent the absorption values of different materials, PBS, and ultrapure H_2O treatment, respectively.

2.11. Cell proliferation and cell scratch assay

Cell proliferation was detected using a RAW264.7-3T3 cell Transwell system. RAW264.7 cells were seeded into the upper chamber of a 24-well Transwell plate at a cell density of 1×10^4 per well. 3T3 cells were seeded into the lower chamber at a cell density of 5×10^3 per well. After 24 h, the upper cells were washed 3 times with PBS. 50 μL gAu–CuS HSs and gAu–CuS CSs (100 μg mL^{-1}) (equivalent Au–CuS) were added along with a 100 μL fresh cell culture medium. The upper chamber is then placed over the lower chamber and incubated for 24 h. The fluorescence images were obtained using an EdU-cell proliferation kit.

Cell scratch experiments were performed in a RAW 264.7-3T3 cell Transwell system. RAW 264.7 cells were seeded in the upper chamber at a cell density of 1×10^4 per well, while 3T3 cells were seeded in the lower chamber of a Transwell system at a cell density of 5×10^3 per well. After overnight incubation, cells were scratched in the lower chamber of the Transwell with a sterile 10 μL pipette tip. It was then rinsed with PBS (three times) to remove streaked cell debris, and serum-free medium was added. The upper chamber was washed three times with PBS, 50 μL of gAu–CuS CSs hydrogel and gAu–CuS HSs hydrogel (50 μg mL^{-1}) were added (equivalent Au–CuS), and 100 μL of fresh medium was added. The upper chamber is then placed over the lower chamber to construct a Transwell system. Bright-field cell pictures were taken with a microscope at different periods (0 h, 24 h).

2.12. Determination of macrophage (RAW 264.7) polarization type

The level of polarization of cells induced by gAu–CuS HSs was investigated in RAW 264.7 cells. Tumor necrosis factor (TNF-α) and interleukin (IL-10) factors were selected to represent the representative factors of macrophage M1 and M2 phenotypes, respectively. The levels of these two factors were characterized

 This journal is © The Royal Society of Chemistry 2023

Open Access Article. Published on 25 2023. Downloaded on 30.5.2026 16:35:55.
This article is licensed under a Creative Commons Attribution-NonCommercial 3.0 Unported Licence.

by the ELISA method. The specific operations are as follows: RAW 264.7 cells were seeded into a 96-well plate at a cell density of 1×10^4 per well. The upper medium was removed after incubating overnight in a cell incubator. Then the gAu–CuS CSs hydrogel and gAu–CuS HSs hydrogel containing different concentrations of Au–CuS NPs (200, 100, 50, 25, 0 μg mL^{-1}) were added. After 48 h of co-incubation, the cell culture plates were centrifuged at 200 rpm for 10 min. Transfer 50 μL of the supernatant to a new ELISA test plate, and detect the levels of two cytokines, TNF-α and IL-10 (according to the manufacturer instructions).

2.13. Hemostatic ability and mouse skin adhesion properties of the gAu–CuS CSs hydrogel and gAu–CuS HSs hydrogel

The hemostatic ability of the gAu–CuS HSs hydrogels was investigated using a diabetic mouse liver hemorrhage model. All animal work was performed following the regulations of the Animal Care and Use Committee of the Suzhou Institute of Nanotechnology and Nanoionics, Chinese Academy of Sciences. First, a type I diabetes model was established using BALB/c male mice (Skorui Biological. Nanjing). Mice were given adequate water and food and kept in a dry environment. Each mouse was injected with streptozotocin (STZ) at 65–75 mg kg^{-1} for 5 consecutive days according to body weight, the mice fasted for 12 h, and the drug was injected intraperitoneally.

After 14 d, blood glucose was measured continuously for one week, and mice with blood glucose levels higher than 16.7 mM were considered diabetic. Mice were anesthetized with inhalation of isoflurane gas anesthesia and then the liver was exposed through an incision in the abdomen, and the surrounding tissue fluid was removed. The liver was punctured with an 18G needle. The gAu–CuS CSs hydrogel and gAu–CuS HSs hydrogel were injected immediately into the bleeding site. The SF–HA hydrogel without Au–CuS NPs was selected as a control. The location of the hepatic hemorrhage was photographed at specific times (0, 15, 30, 60 s).

Test mouse skin adhesion properties: take two skins of male BALB/c mice, drop 20 μL of Au–CuS CSs or Au–CuS HSs, and gAu–CuS CSs hydrogel or gAu–CuS HSs hydrogel and PBS solution into one skin, press with fingers for 30 s, and apply 1 mm min^{-1} testing at a constant rate. For the adhesion test of Au–CuS CSs, Au–CuS HSs, gAu–CuS CSs hydrogel, gAu–CuS HSs hydrogel, and SF–HA hydrogels were injected between two pieces of skin after forming the glue, press for 30 s, and use the instrument to perform the tensile test.

2.14. Histological analysis, immunofluorescence staining, and biochemical analysis

The effect of gAu–CuS HSs hydrogel on diabetic wound healing was evaluated on a full-thickness skin wound model in diabetic male BALB/c mice (20–25 g). First, diabetic mice were anesthetized with isoflurane gas anesthesia, and their backs were shaved to form a circular full-thickness skin wound (10 mm) d. BALB/c mice were randomly divided into 8 equal groups (n = 5 per group): (a) PBS, (b) PBS + light, (c) SF–HA, (d) SF–HA + light, (e) gAu–CuS CSs hydrogel, (f) gAu–CuS CSs hydrogel + light, (g) gAu–CuS HSs hydrogel, and (h) gAu–CuS HSs HSs hydrogel + light. The hydrogels were sterilized using a 200 nm filter before mixing injection, and the Au–CuS NPs suspension was sterilized by autoclaving. A digital camera recorded the wound healing status at different times (0, 3, 7, and 14 d). The wound areas were quantified using Image J software.

For histological analysis, wound tissue from diabetic mice was collected on 14 d, fixed with 4% paraformaldehyde, and the harvested tissue samples were processed, embedded in paraffin, sectioned into pieces, and stained with hematoxylin and eosin (H&E) and Masson's trichrome (MTS) following a standard histological procedure. The stained images were obtained by microscopy. For immunofluorescence staining, wound tissues from diabetic mice were collected on 7 and 14 d, dehydrated and embedded, and then frozen sections were made. Immunofluorescence staining for IL-1β, CD31, F4/80, and CD163 was performed using standard protocols, and immunofluorescence images were obtained by using a fluorescence microscope. Wound tissues from diabetic mice on days 0, 7 and 14 were taken for biochemical analysis. The levels of IL-6, TGF-β, IFN-γ and IL-10 in the wound area were assessed by ELISA. Briefly, the wound tissue was added to 2 mL of cold PBS containing 1% Igepal CA-630 non-ionic detergent. The tissue was then homogenized through a tissue disruptor. After centrifugation at 3000 rpm for 5 min, the supernatant was taken to determine the levels of different factors using ELISA kits.

3. Results and discussion

3.1. Synthesis and characterization of Au–CuS CSs and Au–CuS HSs

This study prepared Au nanorods by seed growth as templates. Subsequently, anisotropic overgrown textured or fully covered smooth-like shapes of CuS on Au nanorods were successfully synthesized by varying the intermediate K_2PtCl_4. K_2PtCl_4 mainly plays dual functional roles in the synthesis, including pre-adsorption on Au NRs to prepare for the growth of Cu^{2+}, and redox reaction with Cu^{2+}. Thus, Au–Cu_2O heterostructures with different surface morphologies can be obtained. Finally, a sulfurization reaction is performed to form Au–CuS nanorods (Au–CuS NRs) by further reacting Au–Cu_2O with sodium sulfide (Na_2S). Transmission electron microscopy (TEM) demonstrated the formation of surface rough mace-like heterostructures (Au–CuS HSs) and smooth surface core–shell structures (Au–CuS CSs), respectively (Fig. 2(A)). The surface of Au–CuS HSs not only has a rough surface texture structure and abundant CuS burrs of about 7.5 nm, but the Au–CuS CSs have a CuS shell of ~3.2 nm. The obtained nanomaterials all have good water solubility, the size range of flow dynamics is 120.7 ± 8.43 to 149.7 ± 15.78 nm (Fig. S1, ESI†), and the Zeta potential in water is −13.7 ± 4.67 to −17.4 ± 3.62 mV (Fig. S2, ESI†). At the same time, good solubility in DMEM facilitates their application at the cellular level (Fig. S3, ESI†). Further analysis by XRD confirmed the successful synthesis of Au–CuS CSs and Au–CuS HSs (Fig. S4, ESI†), both of which have the same crystal structure:

Open Access Article. Published on 25 2023. Downloaded on 30.5.2026 16:35:55.
This article is licensed under a Creative Commons Attribution-NonCommercial 3.0 Unported Licence.

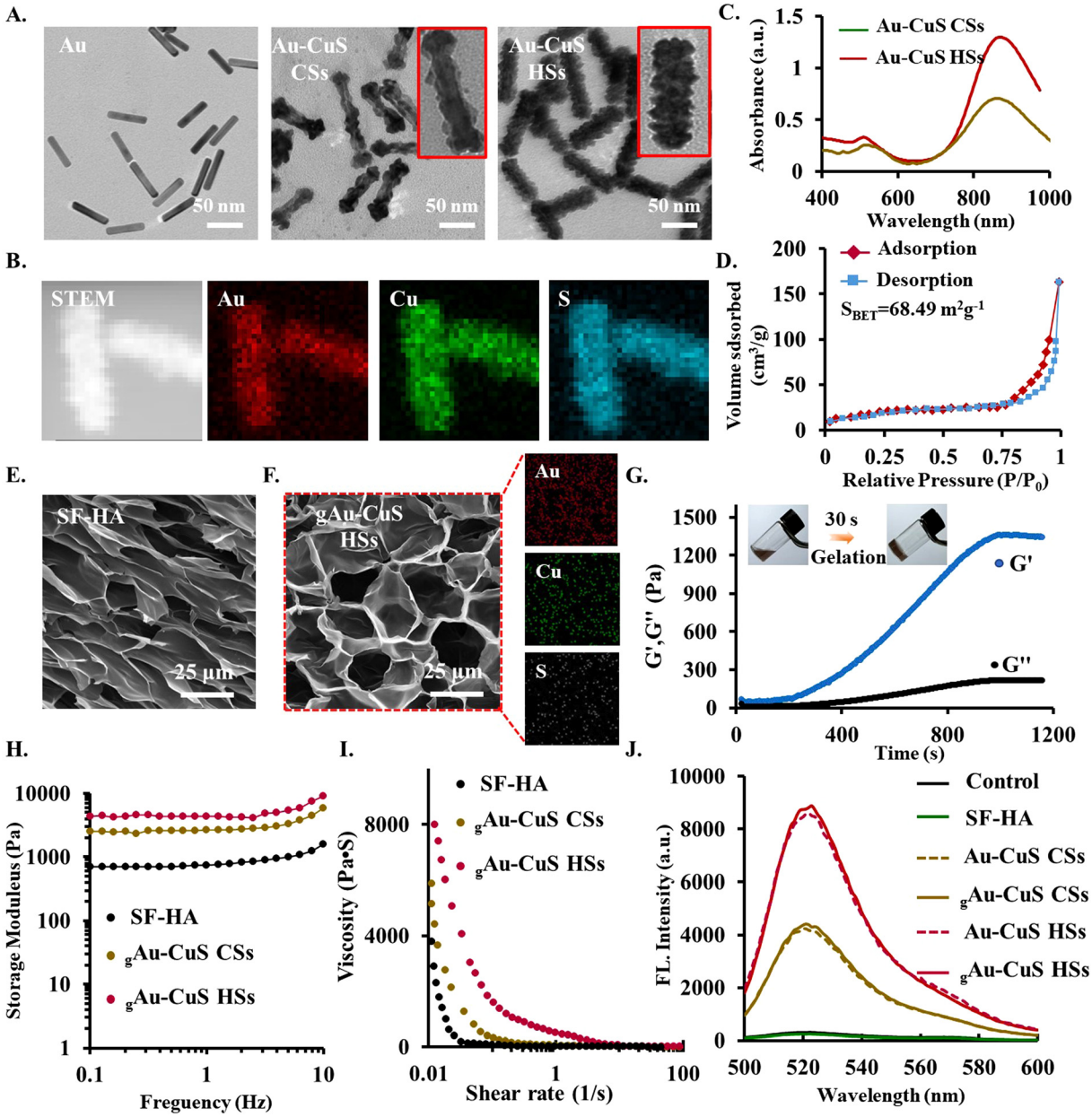

Fig. 2 Synthesis and physicochemical characterization of Au–CuS NRs heterostructure and gAu–CuS NRs hydrogels. (A) TEM of Au NRs; Au–CuS CSs, and Au–CuS HSs. (B) Scanning transmission electron microscopy (STEM) images and EDS elemental mapping images of Au NRs; Au–CuS CSs, and Au–CuS HSs. (C) UV-Vis NIR absorption spectrum of Au–CuS NRs. (D) Determination of the specific surface area of Au–CuS HSs. (E) and (F) Representative SEM micrograph of SF–HA hydrogels and gAu–CuS HSs hydrogels with corresponding EDS mapping. (G) Storage modulus (G') and loss modulus (G'') of the gAu–CuS HSs hydrogel during gelation. Inset: sol–gel transition photograph of the gAu–CuS HSs hydrogel. (H) Storage modulus–strain response patterns of SF–HA, gAu–CuS CSs, and gAu–CuS HSs hydrogels. (I) The viscosity (shear rate = 0.1 to 100 s^{-1}) of SF–HA, gAu–CuS CSs hydrogel, and gAu–CuS HSs hydrogels. (J) Emission spectra of DCF (excited at 455 nm) in PBS containing various gAu–CuS NR hydrogels or Au–CuS NRs under 808 nm laser irradiation (0.75 W cm^{-2}, 10 min).

the cubic phase of Au (JCPDS cards # 04-0784) and the covellite phase of CuS (JCPDS cards # 06-0464). Energy-dispersive X-ray spectroscopy (EDS)-based elemental mapping results confirmed the successful synthesis of mace-like rough Au–CuS HSs material containing Au, Cu, and S elements (Fig. 2(B)). Ultraviolet-visible-near-infrared spectroscopy (UV-Vis-NIR) (Fig. 2(C)) revealed that Au–CuS CSs and Au–CuS HSs exhibited strong absorption peaks in the near-infrared region, which significantly enhanced Au–CuS in the near-infrared region due to the overlap of the LSPRs of Au and CuS (Fig. S5, ESI†), and LSPR absorption in the infrared region. The surface areas of Au–CuS CSs (Fig. S6, ESI†) and Au–CuS HSs (Fig. 2(D)) were obtained by Brunauer–Emmett–Teller (BET) analysis to be 23.16 m^2 g^{-1} and 68.49 m^2 g^{-1}, respectively, further indicating that the designed mace-like rough Au–CuS HSs nanoparticles have a larger surface area.

 This journal is © The Royal Society of Chemistry 2023

Open Access Article. Published on 25 2023. Downloaded on 30.5.2026 16:35:55.
This article is licensed under a Creative Commons Attribution-NonCommercial 3.0 Unported Licence.

3.2. Synthesis and characterization of Au–CuS reinforced injectable hydrogel

HA–Tyr was combined with SF to form injectable hydrogels using an enzyme-mediated cross-linking process using HRP and H_2O_2. SF and HA-based biomaterials emerging as an appealing starting material regulate cellular and biological responses (including cell adhesion, proliferation, differentiation, angiogenesis, and wound healing) in bioengineering due to their good biocompatibility, biodegradability, poor immunogenicity, versatility, and biomimetic properties. The pristine SF hydrogels have enough mechanical strength and a modest degradation rate, while pristine HA hydrogels hold poor mechanical strength and rapid degradation rate. A hybrid hydrogel system composed of HA–Tyr and SF (HA/SF) could hold superior properties and diminish previously described weaknesses using HRP and H_2O_2.[43] To obtain SF–HA hydrogels, tyramine-modified HA (HA–Tyr) was first obtained, followed by the incorporation of 25% SF. The drawback of HA brittleness, which is not ideal for application to the skin, is resolved by the inclusion of SF. Additionally, if there is an excessive amount of SF added, the hydrogel's mechanical characteristics will be too low, which will have an impact on their potential applications (Fig. S7, ESI†). SF–HA hydrogels containing 25% SF were chosen. SF is also rich in Tyr groups, so it can still undergo chemical cross-linking under the combined action of HRP and H_2O_2 to form hydrogels. Hydrogel materials must have a suitable gelation rate, pore size, and mechanical strength to meet practical applications. By adjusting the concentrations of HRP (1 U mL^{-1}) and H_2O_2 (1 mM), the final optimal gel-forming conditions were 2% (w/v) SF–HA. At this time, the hydrogel was cured and formed in about 30 s, with excellent injectable behavior. Subsequently, hyaluronic acid and hyaluronic acid modified with Try were characterized by ^1H NMR spectroscopy. As shown in Fig. S8 (ESI†), the peaks at δ 6.7 ppm and δ 7.2 ppm are characteristic peaks of the benzene ring group in Try, indicating that Try was successfully modified onto HA to obtain the HA-Try material. The grafting rate of HA-Try was calculated to be about 13% by comparison with the peak area of the methyl group in the acetyl group in the HA molecular unit. Furthermore, the morphology of the SF–HA hydrogel was analyzed by scanning electron microscope (SEM) (Fig. 2(E)), 200 μg mL^{-1} of Au–CuS CSs and Au–CuS HSs were selected to be incorporated into the hydrogels. The hydrogel's initial pore size was enlarged by the inclusion of nanoparticles. Furthermore, EDS confirmed the existence of each element of Au–CuS NRs, indicating that Au–CuS CSs (Fig. S9, ESI†) and Au–CuS HSs (Fig. 2(F)) were successfully integrated into the hydrogel network. It was subsequently tested for its rheological properties, and its mechanical properties improved significantly with time, indicating the formation of hydrogels (Fig. 2(G)). Simultaneously, due to the presence of Au–CuS NRs, the mechanical properties of the hydrogels are significantly improved (Fig. 2(H)). In addition to the hydrogel's intrinsic mechanical characteristics, the gelation rate is a crucial consideration when evaluating injectable hydrogels. To achieve a precise fit between the hydrogel and the surrounding native tissue, an appropriate gelation rate is necessary in order to permit the use of tissue engineering to fill irregularly shaped tissue defects before the hydrogel solidifies. Then shear rate-dependent viscosity variations were examined. Remarkably, the viscosity of the gAu–CuS HSs hydrogel dramatically decreased from 8000 Pa s with the shear rate changing from 0.1 to 100 s^{-1}. The incorporation of nanomaterials did not affect the injectable properties of the hydrogel itself (Fig. 2(I)). This shear thinning ability results in significant injectability of the gAu–CuS HSs hydrogel, which may be appreciated in clinical applications.

Overall, by altering the concentration of HRP and the low concentration of H_2O_2, we could modify the gelation time, mechanical strength, gelation characteristics, and adhesion potential of the injectable hydrogels. The hydrogels can rapidly form after injection to prevent uncontrolled leaching of nanoparticles and gel precursors to the surrounding tissues. Furthermore, it can be slowly created to close irregularly shaped wound defects before solidification. It is thus possible to regulate the mechanical characteristics and gelation rate of our new injectable hydrogel, which could be critical for medication delivery and tissue engineering applications.

3.3. ROS generation potential of gAu–CuS CSs and gAu–CuS HSs hydrogel

The strong local electromagnetic field generated around the gold core can be transmitted from the Au core to the peripheral CuS through resonance energy transfer (RET) when the incident light's wavelength coincides with the Au core's LSPR peak. This will considerably encourage the Au–CuS NRs to produce additional ROS. The ability of two Au–CuS NRs to generate ROS under near-infrared illumination was evaluated by DCF assay. Without the addition of an 808 nm laser, the fluorescence intensity of DCF did not increase (Fig. S10, ESI†), indicating that the Au–CuS CSs and Au–CuS HSs did not generate ROS. However, the DCF fluorescence intensities of Au–CuS CSs and Au–CuS HSs were dramatically increased during 808 nm laser irradiation (0.75 W cm^{-2}, 10 min), indicating extensive ROS production in these nanomaterials. Among them, Au–CuS HSs can induce robust DCF fluorescence, which means that Au–CuS HSs can generate a significant amount of ROS. Au–CuS NRs can successfully facilitate the separation of electrons and holes with rough surfaces and burr structures, which are challenging to recombine. Similarly, we examined the ability of Au–CuS to generate ROS after incorporating Au–CuS into the hydrogel. The hydrogel platform does not affect the ROS generation potential of nanomaterials (Fig. 2(J)). The remarkable capacity of gAu–CuS HSs to produce ROS is promising for eradicating microorganisms.

3.4. Nanobridge adhesion effect of gAu–CuS CSs and gAu–CuS HSs hydrogel

The nanobridge adhesion effect was mainly measured by testing the adhesion ability of nanoparticles to skin tissue. PBS, Au–CuS CSs, and Au–CuS HSs were instilled between two pieces

Open Access Article. Published on 25 2023. Downloaded on 30.5.2026 16:35:55.
This article is licensed under a Creative Commons Attribution-NonCommercial 3.0 Unported Licence.

of mouse skin. The state of the two skins was observed after 3 h. It can be seen from Fig. S11 (ESI†) that both Au–CuS CSs and Au–CuS HSs affect skin adhesion, while pure PBS cannot. Additionally, there were notable distinctions between Au–CuS CSs and Au–CuS HSs, with the fact that Au–CuS HSs had the strongest skin adherence. It was then further subjected to tensile testing for shear adhesion. As illustrated in Fig. S12 (ESI†), both Au–CuS NRs can have a clear advantage over PBS regarding skin adhesion, which is because the nanomaterial itself can interact with the skin and create an adhesion force. Furthermore, Au–CuS HSs exhibited more significant displacement distances and robust adhesion properties (Fig. S13, ESI†), attributed to their excellent surface roughness. Au–CuS HSs can act as superior skin adhesives and achieve rapid hemostasis of wounds.

Wound dressings require a satisfactory level of tissue adherence. Fig. 3(A) demonstrates that the hydrogel adheres without release to a fingertip, indicating that the SF–HA hydrogel adheres securely to human skin. In addition, the hydrogel adheres to different substrates, including plastic, further illustrating its excellent adherence (Fig. 3(B)). We further confirmed the nanobridge effect of the hydrogel including gAu–CuS CSs and gAu–CuS HSs, suggesting that the Au–CuS HSs reinforced hydrogel may function as a superior wound healing agent. Fig. 3(C) findings demonstrate that the gAu–CuS CSs hydrogel and gAu–CuS HSs hydrogel continue to have a strong nanobridge effect and show good tensile displacement (Fig. 3(D)). Moreover, the quantitative adhesion strength of the gAu–CuS HSs hydrogel can reach up to 1.78 kPa, which is much greater than that of the control group (0.758 kPa), further verifying its satisfactory adhesiveness (Fig. 3(E)). Due to the advantages of the hydrogel, adding the nanomaterials into the hydrogel did not reduce their ability to generate ROS or adhere to the skin, but rather increased it, and therefore the organic/inorganic hydrogels make it possible to treat large wounds with gAu–CuS HSs hydrogels.

The mouse hemorrhage liver model was used to determine the hemostatic potential of gAu–CuS HSs hydrogels (Fig. 3(F)). Our results demonstrated that the rate of blood loss was much lower in the group treated with the gAu–CuS HSs hydrogel than in the untreated control group. Although the SF–HA hydrogel and gAu–CuS CSs hydrogel groups also showed some reduction in bleeding (Fig. 3(G)). The quick gelation time and good adhesion of gAu–CuS HSs hydrogels may be responsible for their rapid hemostatic characteristics. This is because the hydrogels can cling to the bleeding site and the contained Au–CuS HSs have a mace-like spiky structure on their surface that penetrates deep into the skin, builds a dense barrier at the bleeding defect and then forms the nano bridge effect.

3.5. Antibacterial properties of gAu–CuS CSs and gAu–CuS HSs under NIR irradiation

Wound infection is linked to significant morbidity and mortality and can also lead to bacteremia or sepsis. Herein, we used *E. coli* and *S. aureus* as model bacterial strains to verify the antibacterial ability of the gAu–CuS CSs hydrogel and gAu–CuS HSs hydrogel. First, we discovered that both the gAu–CuS CSs hydrogel and the gAu–CuS HSs hydrogel displayed concentration-dependent antibacterial properties against both bacterial strains under 808 nm laser irradiation (0.75 W cm^{-2}, 10 min), with gAu–CuS HSs exhibiting the more pronounced antibacterial properties (Fig. 4(A) and (C)). In contrast, the gAu–CuS CSs hydrogel and gAu–CuS HSs hydrogel showed no inhibitory effect without exposure to 808 nm laser light (Fig. S14A and S15A, ESI†). Under 808 nm laser irradiation, the corresponding bacterial viability was assessed, and the gAu–CuS HSs hydrogel had good antibacterial efficacy against both bacteria, resulting in 90% bacterial mortality (Fig. 4(B) and (D)). Correspondingly, there is no apparent bacterial killing effect without NIR irradiation (Fig. S14B and S15B, ESI†). To further confirm the antibacterial ability of the gAu–CuS NRs hydrogel, the plate count method evaluated the CFU. Our findings showed that the CFU of *E. coli* and *S. aureus* was greatly reduced following incubation with gAu–CuS HSs hydrogel and 808 nm laser irradiation (0.75 W cm^{-2}, 10 min), with the gAu–CuS HSs hydrogel exhibiting the most effective antibacterial performance (Fig. 4(E)). In the absence of NIR, the antibacterial ability of the used nanomaterials was greatly reduced (Fig. S16, ESI†). SEM was used to investigate the morphology changes of *E. coli* and *S. aureus* after gAu–CuS CSs hydrogel and gAu–CuS HSs hydrogel treatment. The surfaces of *E. coli* and *S. aure*us that were not treated with light and materials were smooth and maintained their characteristic morphology (Fig. S17, ESI†). However, the surface of *E. coli* and *S. aureus* treated with gAu–CuS CSs hydrogel and gAu–CuS HSs hydrogel was severely damaged, became rough and wrinkled, and had bacterial content leaking out after the application of 808 nm laser irradiation (0.75 W cm^{-2}, 10 min). As indicated by the arrows, when the gAu–CuS HSs hydrogel was applied to the bacterial surface, a large number of lysis-like pores appeared on the bacterial surface and the cell membrane structure was most severely damaged (Fig. 4(F)). The results displayed that the gAu–CuS HSs hydrogel outperformed the gAu–CuS CSs hydrogel in antibacterial performance when exposed to 808 nm NIR light, which was attributable to the increased ROS generation. The excellent ROS generation ability of the gAu–CuS CSs hydrogel and gAu–CuS HSs hydrogel under NIR irradiation implied that they could be used to kill bacteria.

3.6. Antibacterial mechanism investigation

The excellent antibacterial properties of the gAu–CuS HSs hydrogel under 808 nm laser irradiation are inseparable from their ROS generation. Therefore, we speculate that oxidative stress is the underlying mechanism for the antibacterial activity of gAu–CuS HSs hydrogel. Herein, we used DCF-DA to detect the ROS production in bacteria, and after 808 nm laser irradiation (0.75 W cm^{-2}, 10 min), the gAu–CuS HSs hydrogel significantly enhanced DCF fluorescence in *E. coli* and *S. aureus* compared to the gAu–CuS CSs hydrogel, demonstrating more ROS production within the bacterial cells (Fig. 4(G) and (H)). In the absence of laser irradiation, the fluorescence of DCF did not increase, indicating that there was not a large amount

 This journal is © The Royal Society of Chemistry 2023

Open Access Article. Published on 25 2023. Downloaded on 30.5.2026 16:35:55.
This article is licensed under a Creative Commons Attribution-NonCommercial 3.0 Unported Licence.

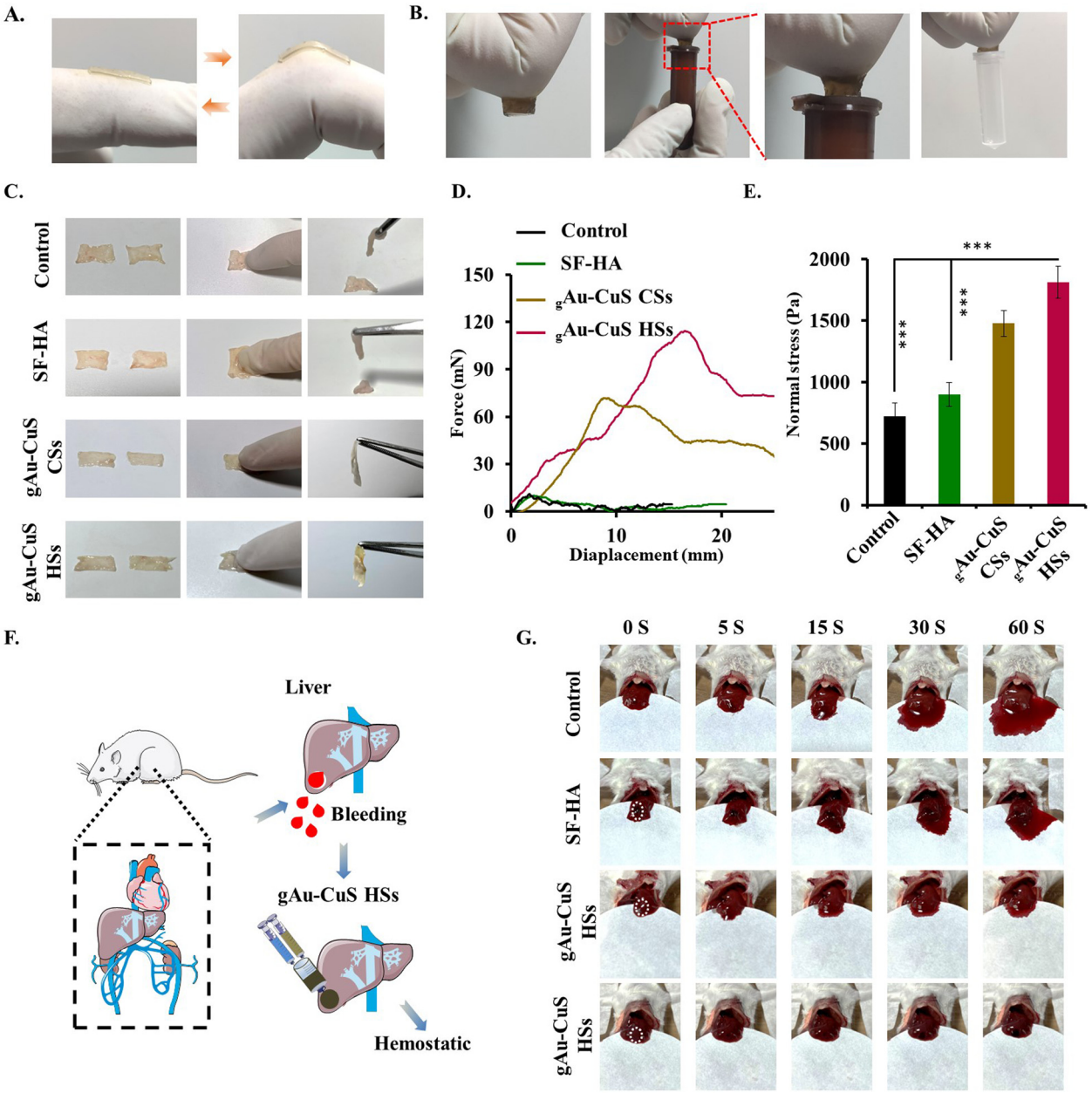

Fig. 3 Detection of nanobridge adhesion properties of gAu–CuS CSs and gAu–CuS HSs hydrogel. (A) Adhesion capacity of SF–HA hydrogels on the fingers. (B) Adhesion capacity of the gAu–CuS HSs hydrogel. (C) Adhesion properties of the gAu–CuS CSs and gAu–CuS HSs hydrogel on two pieces of mouse skin. (D) Force–displacement curves for the lap joints of two mouse skins that were bonded together using gAu–CuS CSs and gAu–CuS HSs hydrogels. (E) A lap-shear test was utilized to examine the adhesive power of gAu–CuS CSs and gAu–CuS HSs hydrogel concerning skin tissue. (F) Diagrammatic representation of the hemostatic properties of gAu–CuS CSs and gAu–CuS HSs hydrogel against the diabetic mice liver hemorrhaging model. (G) Representative photograph of diabetic mice livers with the different treatments at 0, 5, 15, 30, and 60 s after being exposed to 50 μg mL^{-1} gAu–CuS CSs and gAu–CuS HSs hydrogels (equivalent to Au–CuS). (***$p < 0.001$, **$p < 0.01$, *$p < 0.05$).

of ROS production in the bacteria under dark conditions (Fig. S18, ESI†).

Excessive ROS will break the original redox balance of the organism and destroy the antioxidant system, which will lead to high levels of oxidative stress. Oxidative stress will directly lead to the consumption of GSH, which will be toxic to the microbial cells and induce death. Therefore, GSH levels were examined in bacteria. Fig. 4(I) and (J) manifested the gAu–CuS HSs hydrogel caused a significant GSH decrease in both *E. coli* and *S. aureus* under 808 nm laser irradiation, similar to the increasing trend of ROS mentioned above (0.75 W cm^{-2}, 10 min). Similarly, GSH levels did not change without laser irradiation (Fig. S19, ESI†). In addition, ROS can oxidize the unsaturated fatty acids on bacterial membranes, leading to lipid peroxidation. The lipid peroxidation in bacteria was assessed by detecting the malondialdehyde (MDA) level in the bacteria. Fig. 4(K) and (L) indicated that when bacteria were exposed to 808 nm laser irradiation, the gAu–CuS HSs hydrogel produced more MDA than the gAu–CuS CSs hydrogel.

Open Access Article. Published on 25 2023. Downloaded on 30.5.2026 16:35:55.
This article is licensed under a Creative Commons Attribution-NonCommercial 3.0 Unported Licence.

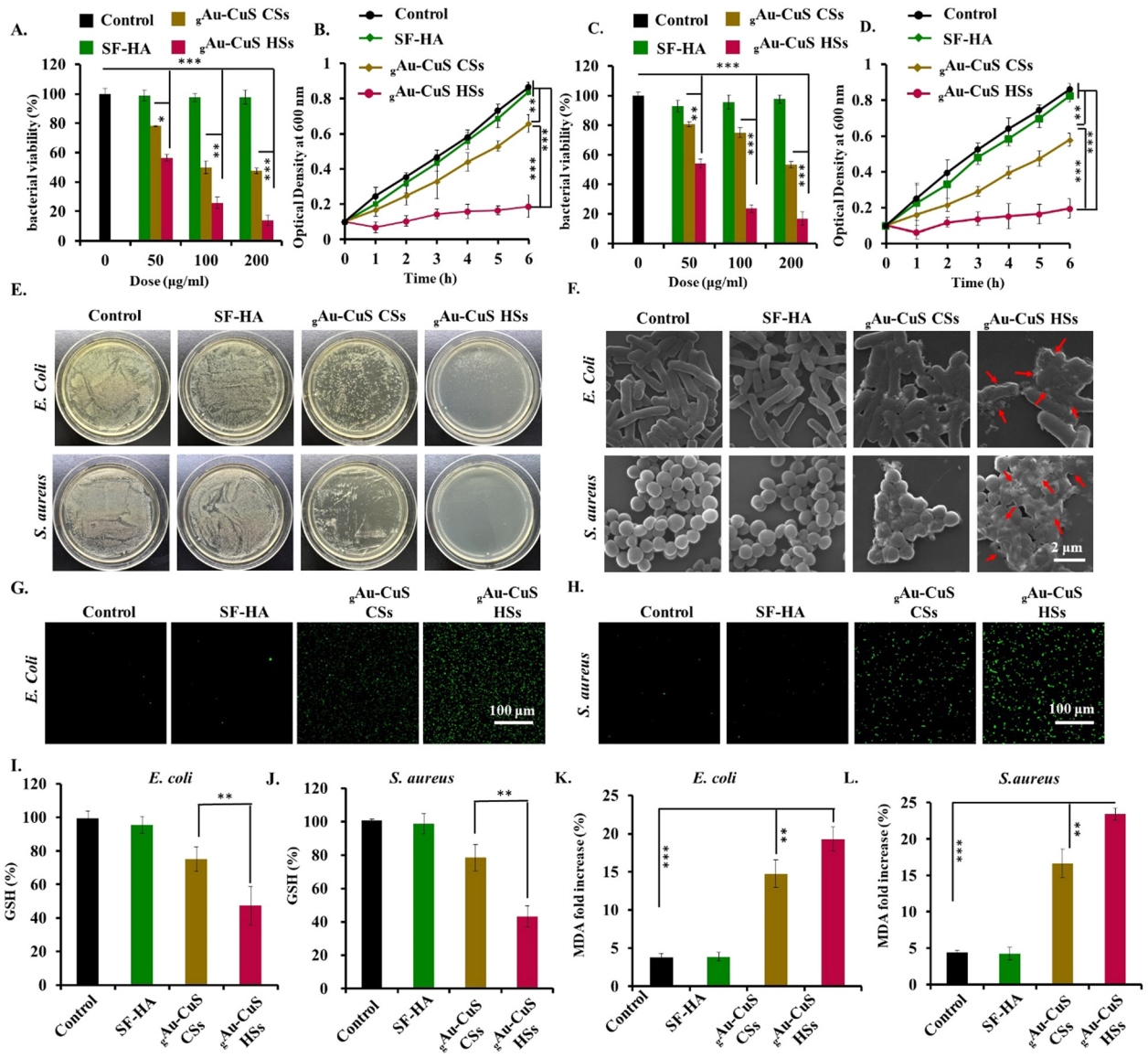

Fig. 4 Antibacterial performance of gAu–CuS CSs and gAu–CuS HSs hydrogels. Antibacterial activity with different concentrations of Au–CuS CSs hydrogels and Au–CuS HSs hydrogel (equivalent to Au–CuS) against *E. coli* (A) and *S. aureus* (C). Absorbance at 600 nm of *E. coli* (B) and *S. aureus*. (D) Treatment with Au–CuS CSs hydrogels and Au–CuS HSs hydrogels for different periods. (E) Antibacterial potential of different treatment groups against *E. coli* and *S. aureus* on agar plates. (F) SEM micrograph of *E. coli* and *S. aureus*. (G) and (H) Characterization of the fluorescence intensity of DCF (excited at 455 nm) in *E. coli* and *S. aureus*. (I)–(L) GSH levels and lipid peroxidation levels in *E. coli* and *S. aureus*. For (A)–(K), *E. coli* and *S. aureus* were incubated with various concentrations (A), (C) or 50 μg mL^{-1} (B), (D), (E)–(L) gAu–CuS CSs and gAu–CuS HSs hydrogels (equivalent to Au–CuS) 6 h, then 10 min with an 808 nm laser at 0.75 W cm^{-2}, followed by additional incubations (***$p < 0.001$, **$p < 0.01$, *$p < 0.05$).

In the absence of laser irradiation, there was no abundant MDA production, which indicated no bacterial lipid peroxidation (Fig. S20, ESI†). Therefore, we concluded that the superior antibacterial activity of gAu–CuS HSs under 808 nm laser irradiation due to the activation of oxidative stress pathways inside bacteria.

3.7. *In vitro* macrophage polarization of the gAu–CuS HSs hydrogel

The biocompatibility of hydroges systems containing different Au–CuS NR materials (gAu–CuS NRs) was assessed by (3-(4,5-dimethyl-2-thiazoLyl)-2,5-diphenyl tetrazolium bromide) (MTT) assay and live/dead staining. gAu–CuS NRs were co-incubated with mouse fibroblasts (NIH-3T3). Neither the experimental group nor the control group showed any toxicity after 72 h of incubation (Fig. S21A, ESI†). Afterward, the morphology of the cells was observed using live (stained green)/dead (stained red) staining. Fig. S21B (ESI†) shows 3T3 cells kept their normal shape after 24 h and 48 h of incubation. The gAu–CuS NRs hydrogel displayed the same cell growth trend as the control group. It maintains more than 98% cellular activity even for up to 72 h, which can be well used for the long-term repair process of skin tissues. In order to better apply it to the organism, we performed hemolysis experiments with different groups. The low hemolysis ratio was found in both Au–CuS NRs and

 This journal is © The Royal Society of Chemistry 2023

Open Access Article. Published on 25 2023. Downloaded on 30.5.2026 16:35:55.
This article is licensed under a Creative Commons Attribution-NonCommercial 3.0 Unported Licence.

gAu–CuS NRs hydrogels, which can be attributed to the remarkable antibacterial capacity and good biocompatibility of these materials (Fig. S22, ESI†), indicating their excellent hemocompatibility. As a result, we conclude that gAu–CuS CSs and gAu–CuS HSs have excellent biocompatibility and are highly safe for tissue engineering applications.

The prohealing M2-polarized macrophage could be crucial for cell proliferation, angiogenesis, vascularization, collagen deposition, and positively impact wound healing. Our study highlighted that NRs with a high surface roughness could modulate the macrophage polarization to the M2 phenotype. The macrophage polarizing ability of the gAu–CuS HSs hydrogel was investigated in mouse macrophages (RAW264.7). The expression levels of TNF-α (M1 phenotype marker) and IL-10 (M2 phenotype marker) in cells were assessed using an ELISA method (Fig. 5(B) and Fig. S23A, ESI†). As depicted in Fig. 5(C) and Fig. S23B (ESI†), only gAu–CuS HSs hydrogels resulted in a significant and concentration-dependent increase in IL-10 levels, however, this phenomenon was not found in gAu–CuS hydrogels, indicating that gAu–CuS HSs hydrogels can directly polarize macrophages to the M2 state. This change is attributed to the rough surface texture-like structure of the incorporated Au–CuS HSs. Notably, the Au–CuS NRs hydrogel had a negligible influence on TNF-α expression under illumination, which was attributable to the fact that the ROS created after NIR illumination affected macrophage phenotypes. Therefore, we concluded that the difference in hydrogel-incorporated nanomaterials caused the difference in macrophage polarization, and this difference could be due to the unique surface roughness of the Au–CuS HSs compared to Au–CuS CSs.

3.8. *In vitro* cell migration and proliferation capacity of the gAu–CuS HSs hydrogel

The M2-polarized macrophage phenotype has the potential to induce favorable effects on both the migration and proliferation of cells. During the proliferative wound healing phase, we hypothesized that gAu–CuS HSs with the potential to polarize macrophages might stimulate cell migration and proliferation. The wound microenvironment was simulated using the RAW264.7-3T3 Transwell system, in which RAW 264.7 cells were seeded in the upper chamber and 3T3 cells were seeded in the lower chamber (Fig. 5(A)). RAW264.7 cells in the upper chamber were co-incubated with the gAu–CuS CSs hydrogel or gAu–CuS HSs hydrogel (50 μg mL^{-1}), allowing cytokines produced in the upper chamber to act on 3T3 cells in the lower chamber. Fig. 5(D) displayed that the gAu–CuS HSs group better-accelerated cell migration compared to the gAu–CuS CSs and control group. The healing rate of scratches at 24 h

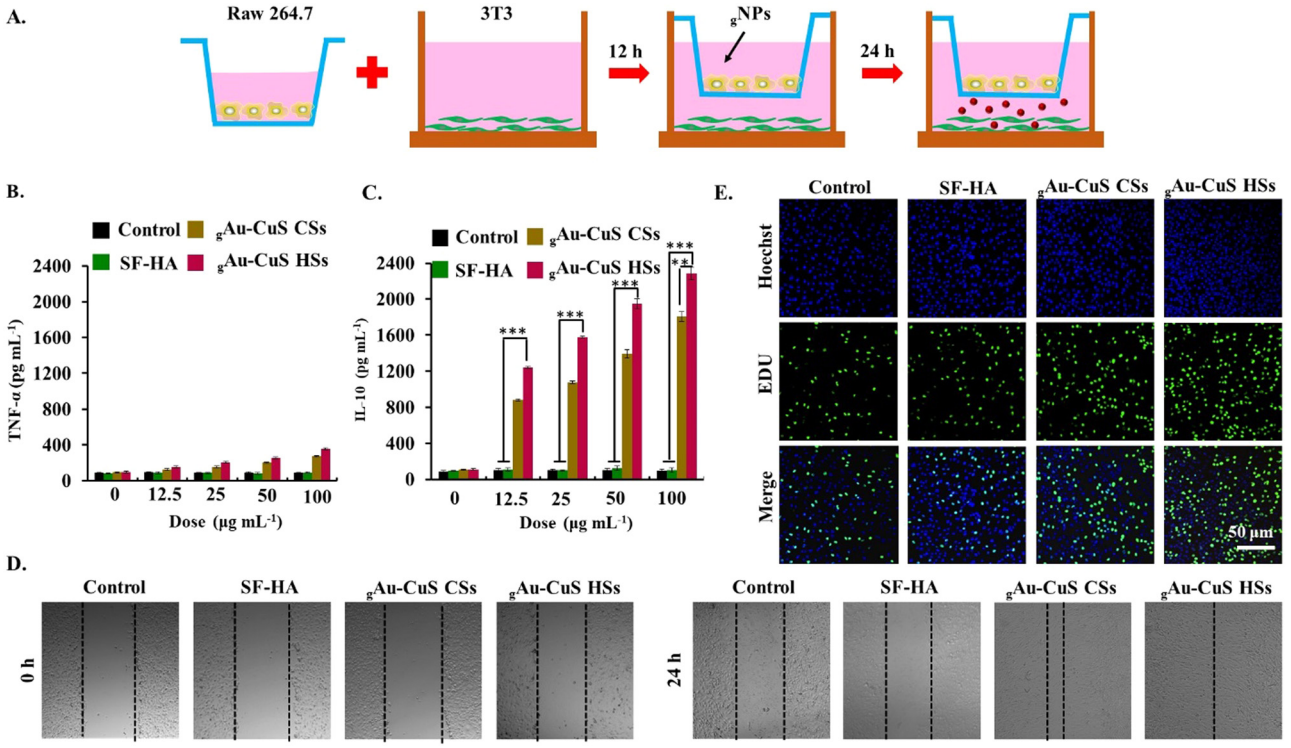

Fig. 5 Cytocompatibility, cell proliferation, and macrophage polarization potential of gAu–CuS NRs hydrogels. (A) Schematic diagram of the Transwell system to simulate the microenvironment of the wound site. TNF-α factor (B) TNF-α expression levels in RAW 264.7 cells. (C) IL-10 expression levels in RAW 264.7 cells. (D) 24 h cell migration level was analyzed by cell scratch analysis that was cultivated with 100 μg mL^{-1} gAu–CuS CSs and gAu–CuS HSs hydrogel (equivalent to Au–CuS). (E) EdU assay was used to measure the growth of 3T3 cells in the RAW 264.7-3T3 transwell system that were grown in 100 g mL^{-1} gAu–CuS CSs hydrogel or gAu–CuS HSs hydrogel (equivalent to Au–CuS) for 24 h. For (B)–(E), cells were incubated with various concentrations of gAu–CuS CSs hydrogel, and gAu–CuS HSs hydrogel for 6 h, an 808 nm laser at 0.75 W cm^{-2} was then used for 10 min, followed by additional incubations (***$p < 0.001$, **$p < 0.01$, *$p < 0.05$).

Open Access Article. Published on 25 2023. Downloaded on 30.5.2026 16:35:55.
This article is licensed under a Creative Commons Attribution-NonCommercial 3.0 Unported Licence.

was close to 90%. Even in the dark state, the cells treated with gAu–CuS HSs hydrogel achieved optimal cell migration (Fig. S24, ESI†). This accelerated wound-healing response was mediated by gAu–CuS HSs hydrogel polarizing macrophages to M2. The cell-proliferative ability of gAu–CuS NRs was further examined using the EdU-488 cell proliferation assay. Based on our results in Fig. 5(E) and Fig. S25 (ESI†), 3T3 cells treated with gAu–CuS CSs or gAu–CuS HSs showed more EdU-positive cells than untreated cells, among them, gAu–CuS HSs induced the most EdU positive cells compared with gAu–CuS CSs treatments. This result implies that gAu–CuS HSs can effectively promote cell proliferation and migration during the proliferative stage, therefore accelerating wound healing.

3.9. *In vivo* diabetic wound healing assessment

Inspired by the effective wound closure, inactivation of pathogenic bacterial species, cell migration, and cell proliferation of gAu–CuS HSs hydrogel, the efficacy of the gAu–CuS HSs hydrogel against *in vivo* reconstruction of full-thickness diabetic wound model was investigated. Animal models of diabetes induced by streptozotocin (STZ) have been widely used to study the therapeutic model of diabetic wounds (Fig. 6(A)). The STZ drug was injected intraperitoneally for five consecutive days, and the blood glucose level of the BALB/c mice was monitored. Mice whose blood glucose exceeded 300 mg dL^{-1} (16.65 mmol L^{-1}) for two consecutive weeks were used to treat diabetic wounds. To demonstrate that the gAu–CuS HSs hydrogel can perform programmed wound healing, we divided mice into four groups for comprehensive experiments, including (i) 30 μL of PBS as a control; (ii) 30 μL of SF–HA hydrogel; (iii) hydrogels incorporated with Au–CuS CSs (gAu–CuS CSs hydrogel); (iv) hydrogels incorporated with Au–CuS HSs (gAu–CuS HSs hydrogel). In addition, mice were split into 808 NIR illumination and non-NIR illumination groups.

The hydrogel was injected directly into the full-thickness wound surface, and 12 h later, 808 nm near-infrared light was applied to the wound site (0.75 W cm^{-2}, 10 min). In sustained wound healing experiments, wounds treated with gAu–CuS CSs and gAu–CuS HSs hydrogel exhibited a significantly accelerated wound healing (Fig. 6(B) and (C)). gAu–CuS CSs hydrogel and gAu–CuS HSs hydrogel resulted in 68.5% and 78.5% of wound closures at 7 d, respectively. These percentages were significantly more significant than the control group (32.5%) and SF–HA group (50.7%). Furthermore, the wounds treated with gAu–CuS HSs hydrogel had the best healing effect (97.5%) 14 d after light exposure (Fig. 6(D)) compared to the non-irradiation group in which the gAu–CuS HSs hydrogel results in 25% wound closure at 14 d. Notably, under dark conditions, the wound-healing effect of the gAu–CuS HSs hydrogel was still better than other experimental groups (Fig. S26, ESI†). This could be due to the unique surface rough structure of Au–CuS HSs in the hydrogel, which was proposed to participate in the later wound healing. These results suggested that gAu–CuS HSs under light can accelerate diabetic wound healing.

3.10. Histological evaluation of wound healing performance

Wound healing is a complex physiological process facilitated by the co-ordinated combination of numerous biological and molecular systems. At the end of 14 d of treatment, the regenerated tissues were histologically stained with H&E and MTS to assess the healing impact of gAu–CuS HSs hydrogel on diabetic wounds. Fig. 6(E) shows that after 14 days of treatment, there were still blood scabs and dead inflammatory cells in the PBS group and SF–HA-treated controls, which shows that the wounds took longer to heal. In contrast, wounds treated with gAu–CuS CSs hydrogel and gAu–CuS HSs hydrogel had intact epithelial tissue and more granulation tissue, with gAu–CuS HSs hydrogel's granulation tissue reaching 120 μm (Fig. 6(F)). At the same time, compared with the no-light condition, the tissue collected in the gAu–HSs hydrogel group showed excellent tissue structure, and increased presence of hair follicles and blood vessels compared to counterpart groups (Fig. S27, ESI†). In addition, MTS was carried out to detect the qualitative and quantitative deposition of nascent collagen matrix in the injured area of the skin.

The collagen deposition of the gAu–CuS HSs hydrogel at 14 d was significantly higher than other groups (Fig. 6(G) and Fig. S28, ESI†). It is important to note that the gAu–CuS HSs hydrogel group exhibits the densest collagen deposition when exposed to light (Fig. 6(H)), suggesting that the nanomaterialized hydrogel speeds up wound healing by encouraging collagen deposition.

Accelerated angiogenesis is critical in diabetic wound healing because it provides oxygen and nutrients to damaged tissue and maintains newly formed granulation tissue. Here, newly formed blood vessels at the wound were stained with CD31 (green fluorescence). As illustrated in Fig. 7(A), almost no green fluorescence was noticed in the untreated and pure hydrogel groups. Meanwhile, the green fluorescence intensity increased significantly after the addition of nanomaterials, among which the gAu–CuS HSs hydrogel under NIR light exhibited the highest expression of CD31 about 7.18 folds higher than that of the untreated group (Fig. 7(B)) and 3.1 times higher than the unirradiated gAu–CuS HSs hydrogel group (Fig. S29, ESI†). It was shown that the gAu–CuS HSs hydrogel remodeled the vascular structure and promoted wound healing. At the same time, the skin tissue samples on day 3 were taken for 1L-1β immunofluorescence staining to study the anti-inflammatory effect of the designed material against diabetic wounds. As shown in Fig. 7(C), the incorporation of nanoparticles can inhibit the expression of 1L-1β, and the inhibition effect is better after illumination. Among them, the gAu–CuS HSs hydrogel after irradiation achieved the highest inhibitory effect, which is 12 times lower than the untreated group (Fig. 7(D)), and much lower than the unilluminated group (Fig. S30, ESI†). It was demonstrated that the gAu–CuS HSs hydrogel effectively reduced inflammation during the previous treatment. To find out more about how the gAu–CuS HSs hydrogel changes cells, F4/80 and CD163 immunofluorescence staining was carried out on the wound tissue. As displayed in Fig. 7(E) and Fig. S31 (ESI†), most macrophages were not converted to M1 phenotype

 This journal is © The Royal Society of Chemistry 2023

Open Access Article. Published on 25 2023. Downloaded on 30.5.2026 16:35:55.
This article is licensed under a Creative Commons Attribution-NonCommercial 3.0 Unported Licence.

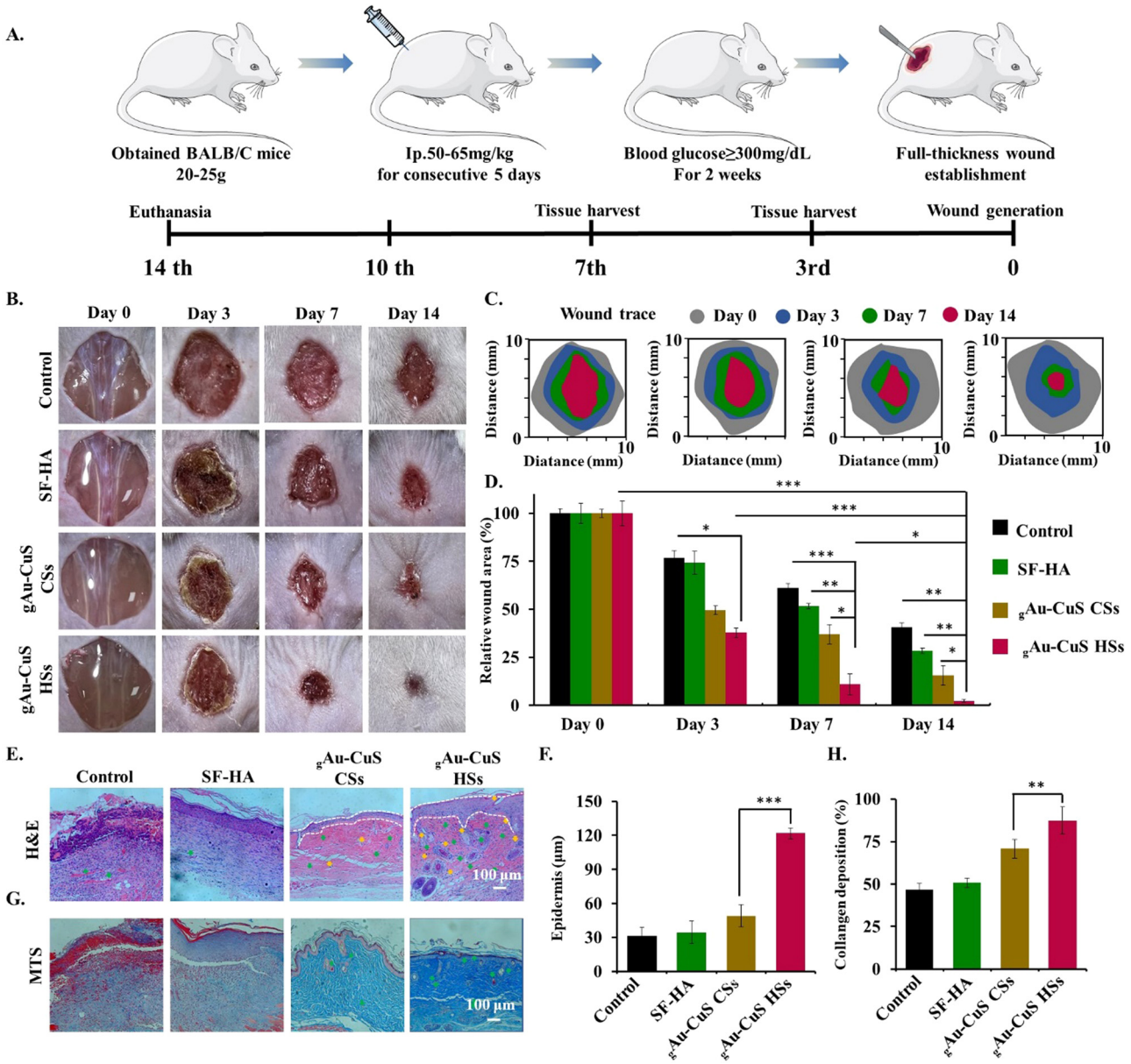

Fig. 6 The gAu–CuS HSs hydrogel accelerated diabetic wound healing in the mice model. (A) The schematic illustration of treatment groups and treatment conditions for diabetic chronic wounds. (B) Photographs depicting the healing of chronic diabetic wounds concerning several treatment groups. (C) Signs of wound-bed closure for each therapy for different periods. (D) *In vivo* wound closure percentage in the mice model at different time points for different treatment groups. (E) H&E staining of wound tissue at 14 d. (F) Quantification of granulation tissue thickness on 14 d. (G) MTS was a stained image of wound tissue. (H) Quantification of collagen. For (B)–(H), animals were incubated with 100 μg mL^{-1} gAu–CuS CSs and gAu–CuS HSs hydrogel (equivalent to Au–CuS) for 6 h, an 808 nm laser at 0.75 W cm^{-2} for 10 min. Green and yellow arrows, and white dashed lines represent vessels, hair follicles, and the boundary of epithelium and dermis, respectively (***$p < 0.001$, **$p < 0.01$, *$p < 0.05$).

under both light and no-light conditions. The M2 phenotype was detected in the collected tissues after applying gAu–CuS HSs hydrogel (CD206) and was remarkably enhanced in comparison to the other condition groups. The red fluorescence of the M2 phenotype was also observed in the gAu–CuS CSs hydrogel-treated wound, but its intensity and area were inferior to those of the gAu–CuS HSs hydrogel group, suggesting that Au–CuS HSs nanomaterials may be more effective at promoting macrophage polarization towards M2 than gAu–CuS CSs. Additionally, the gAu–CuS HSs hydrogel group's fluorescence intensity under non-illuminated conditions is still greater than that of the gAu–CuS CSs hydrogel group, encouraging M2 polarization of macrophages. This is due to the unique surface rough structure of Au–CuS HSs.

Cytokines are crucial to various stages of the wound healing. Wound tissues were collected at 7 d and 14 d after various treatments to verify the anti-inflammatory and wound healing mechanism of the gAu–CuS HSs hydrogel. An ELISA method was used to explore the expression of IL-6, TGF-β1, interferon γ (INF-γ), and IL-10. After skin damage, the pro-inflammatory

Open Access Article. Published on 25 2023. Downloaded on 30.5.2026 16:35:55.
This article is licensed under a Creative Commons Attribution-NonCommercial 3.0 Unported Licence.

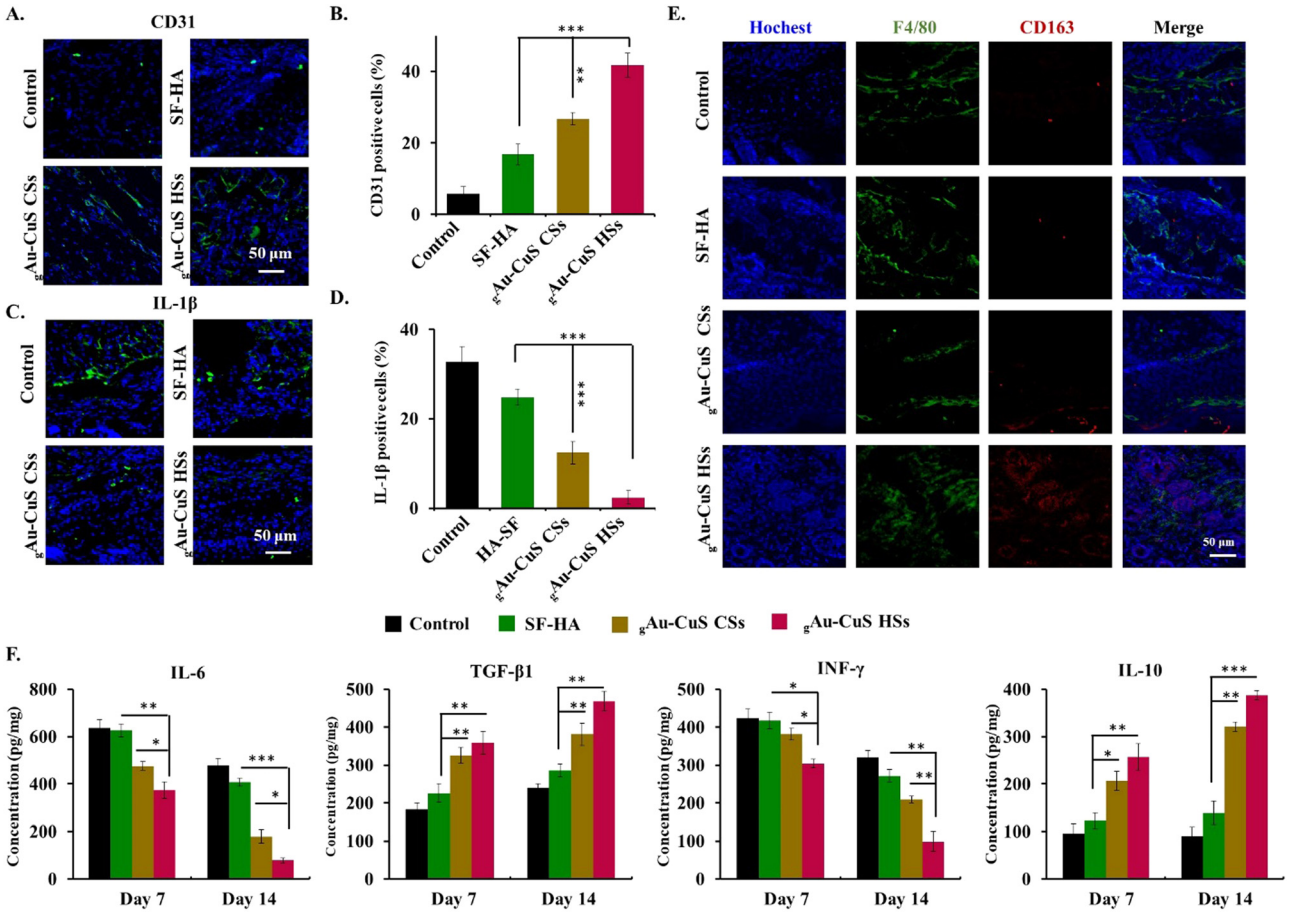

Fig. 7 gAu–CuS HSs hydrogel regulates the wound microenvironment and facilitates chronic diabetic wound healing. (A) Immunofluorescence CD31 (green) staining and nuclei (blue) staining at 14 d. (B) Quantitative evaluation of the relative CD31 coverage area for different treatment groups at different periods. (C) Immunofluorescence micrograph of IL-1β (green) and nuclei (blue) in wound tissues on the 3rd day concerning different treatment groups. (D) Quantitative evaluation of the relative IL-1β coverage area concerning different treatment groups. (E) Immunofluorescence micrographs of macrophages in wound tissue after treatment were stained with F4/80 (green), CD163 (red), and Hoechst (blue). (F) ELISA measured the quantities of chemokines related to inflammation and angiogenesis in wounded skin tissues after different treatments (n = 3) (***$p < 0.001$, **$p < 0.01$, *$p < 0.05$).

IL-6 is thought to be the initiator of promoting inflammation. ELISA results showed that under near-infrared light (Fig. 7(F)), the IL-6 level in the wounds of the gAu–CuS HSs hydrogel group was significantly lower than control groups during the whole healing process. At the same time, the IL-6 level of the gAu–CuS HSs hydrogel under illumination was still lower than under non-illumination conditions (Fig. S32, ESI†). Lowering IL-6 levels can increase fibroblast migration and proliferation while increasing extracellular matrix synthesis.[44–46] TGF-β1 is a well-known cellular immune factor that enhances the wound inflammatory milieu by inducing cell M2 polarization and is involved in cell differentiation, tissue healing, and angiogenesis.[47] The ELISA results showed that the gAu–CuS HSs hydrogel treatment intensely increased TGF-β1 expression (458.9 pg mg^{-1}) which is superior to that of the gAu–CuS CSs hydrogel (371.2 pg mg^{-1}) and the control group (239.4 pg mg^{-1}), which was is more than the non-lighting group. INF-γ is a cytokine that can inhibit the growth of fibroblasts and synthesis of collagen synthesis under *in vitro* conditions. The results displayed that INF-γ decreases throughout the wound healing procedure and the gAu–CuS HSs hydrogel group after the light has maintained the lowest level. IL-10 is the main regulator of inflammation and wound healing because it stops the production of pro-inflammatory factors (IL-6 and IL-8) and reduces the migration of inflammatory cells (*i.e.*, monocytes, macrophages). As expected, the gAu–CuS HSs hydrogel under light can significantly increase the level of IL-10. The content of IL-10 (387.4 pg mg^{-1}) in the gAu–CuS HSs treatment group was about 1.2 fold higher than the gAu–CuS CSs group (300.8 pg mg^{-1}) and 3.2 fold that of the control treatment group (120.9 pg mg^{-1}), indicating that the gAu–CuS HSs hydrogel after light can better accelerate wound healing than counterpart treatment.

Overall, these results indicated that the gAu–CuS HSs group exhibited a decreased expression level of IL-6, INF-γ, and IL-1β, increased expression level of TGF-β1, and IL-10, and could promote naive macrophages to the M2 polarization which is favorable for closure of chronic wounds.

3.11. *In vivo* assessment of long-term systemic toxicity

In tissue engineering and biomedical applications, the biosafety of therapeutic materials at the wound site is critical.

 This journal is © The Royal Society of Chemistry 2023

Open Access Article. Published on 25 2023. Downloaded on 30.5.2026 16:35:55.
This article is licensed under a Creative Commons Attribution-NonCommercial 3.0 Unported Licence.

The long-term toxicity of the gAu–CuS HSs hydrogel *in vivo* was conducted using a mice model. No unexpected changes in the mice's health or behavior were seen during the diabetic wound therapy. The different tissues of mice (heart, liver, spleen, lung, and kidney) at the end of 20 days of therapy were taken for H&E staining. The results showed no damage to major organs in each treatment group under light and non-light exposure conditions (Fig. S33 and S34, ESI†). The results indicated that the introduced materials can be effective programs to promote wound healing and have good biocompatibility and safety profile.

4. Conclusion

Due to numerous interrelated factors that contribute to non-healing wounds, single or dual-function composite systems fail to enhance the overall condition of the wound. Herein, we synthesized mace-like rough nano-heterostructure Au–CuS particles for the first time and designed an injectable all-in-one programmed multi-stage hydrogel composite for diabetic wound healing. The addition of an injectable hydrogel is beneficial to the application of large-scale wounds, while nano-heterostructure particles with rough surfaces showed an excellent nano-bridge effect at the early stage of the wound. The Au–CuS nano-heterostructure exhibited antibacterial ability under near-infrared illumination by promoting the generation of oxygen radicals. In addition, in a mouse liver injury model the gAu–CuS HSs hydrogel exhibited a strong hemostatic effect. The mace-like rough topography induced macrophage polarization towards the M2 phenotype, which is critical for accelerating the healing process. The gAu–CuS HSs hydrogel material integrates various functions to reduce the inflammatory response, stimulate angiogenesis, accelerate cell proliferation, promote granulation formation, exhibit antibacterial potential, and therefore, show excellent acceleration potential to reconstruct diabetic wounds. This study provides the theoretical and experimental reference for designing novel multifunctional nanomaterials and procedural strategies to promote diabetic wound healing.

Author contributions

L. Wang and R. Pei conceived this work, and designed the experiments. L. Wang, Z. Hussain, P. Zheng, and Z. Zhang carried out the characterization of gAu–CuS CSs and gAu–CuS HSs, L. Wang, Y. Zhang, and Y. Cao carried out the synthesis of hydrogels. L. Wang, and Y. Zhang performed the biological assessments. All authors discussed the results and commented on the manuscript.

Conflicts of interest

There are no conflicts to declare.

Acknowledgements

This work was financially supported by the Strategic Priority Research Program of Chinese Academy of Sciences (XDA16040700), and the National Natural Science Foundation of China (31971326, 22177129).

References

1 S. L. Wong, M. Demers, K. Martinod, M. Gallant, Y. M. Wang, A. B. Goldfine, C. R. Kahn and D. D. Wagner, Diabetes primes neutrophils to undergo NETosis, which impairs wound healing, *Nat. Med.*, 2015, **21**(7), 815–819.
2 V. Falanga, Wound healing and its impairment in the diabetic foot, *Lancet*, 2005, **366**(9498), 1736–1743.
3 D. G. Armstrong, A. J. M. Boulton and S. A. Bus, Diabetic Foot Ulcers and Their Recurrence, *N. Engl. J. Med.*, 2017, **376**(24), 2367–2375.
4 N. K. Rajendran, S. S. D. Kumar, N. N. Houreld and H. Abrahamse, A review on nanoparticle based treatment for wound healing, *J. Drug Delivery Sci. Technol.*, 2018, **44**, 421–430.
5 G. C. Gurtner, S. Werner, Y. Barrandon and M. T. Longaker, Wound repair and regeneration, *Nature*, 2008, **453**(7193), 314–321.
6 A. Meddahi-Pelle, A. Legrand, A. Marcellan, L. Louedec, D. Letourneur and L. Leibler, Organ repair, hemostasis, and in vivo bonding of medical devices by aqueous solutions of nanoparticles, *Angew. Chem., Int. Ed.*, 2014, **53**(25), 6369–6373.
7 M. Parani, G. Lokhande, A. Singh and A. K. Gaharwar, Engineered Nanomaterials for Infection Control and Healing Acute and Chronic Wounds, *ACS Appl. Mater. Interfaces*, 2016, **8**(16), 10049–10069.
8 S. Werner and R. Grose, Regulation of wound healing by growth factors and cytokines, *Physiol. Rev.*, 2003, **83**(3), 835–870.
9 C. J. Ferrante and S. J. Leibovich, Regulation of Macrophage Polarization and Wound Healing, *Adv. Wound Care*, 2012, **1**(1), 10–16.
10 P. Krzyszczyk, R. Schloss, A. Palmer and F. Berthiaume, The Role of Macrophages in Acute and Chronic Wound Healing and Interventions to Promote Pro-wound Healing Phenotypes, *Front. Physiol.*, 2018, **9**, 419.
11 A. Mantovani, A. Sica, S. Sozzani, P. Allavena, A. Vecchi and M. Locati, The chemokine system in diverse forms of macrophage activation and polarization, *Trends Immunol.*, 2004, **25**(12), 677–686.
12 G. S. A. Boersema, N. Grotenhuis, Y. Bayon, J. F. Lange and Y. M. Bastiaansen-Jenniskens, The Effect of Biomaterials Used for Tissue Regeneration Purposes on Polarization of Macrophages, *BioRes. Open Access*, 2016, **5**(1), 6–14.
13 M. L. Novak and T. J. Koh, Macrophage phenotypes during tissue repair, *J. Leukocyte Biol.*, 2013, **93**(6), 875–881.
14 Y. N. Zhu, J. M. Zhang, J. Y. Song, J. Yang, Z. Du, W. Q. Zhao, H. S. Guo, C. Y. Wen, Q. S. Li and X. J. Sui, *et al.*,

Open Access Article. Published on 25 2023. Downloaded on 30.5.2026 16:35:55.
This article is licensed under a Creative Commons Attribution-NonCommercial 3.0 Unported Licence.

A Multifunctional Pro-Healing Zwitterionic Hydrogel for Simultaneous Optical Monitoring of pH and Glucose in Diabetic Wound Treatment, *Adv. Funct. Mater.*, 2020, **30**(6), 1905413.

15 R. A. Wimmer, A. Leopoldi, M. Aichinger, N. Wick, B. Hantusch, M. Novatchkova, J. Taubenschmid, M. Hammerle, C. Esk and J. A. Bagley, *et al.*, Human blood vessel organoids as a model of diabetic vasculopathy, *Nature*, 2019, **565**(7740), 505–515.

16 J. Tian, K. K. Y. Wong, C.-M. Ho, C.-N. Lok, W.-Y. Yu, C.-M. Che, J.-F. Chiu and P. K. H. Tam, Topical delivery of silver nanoparticles promotes wound healing, *ChemMedChem*, 2007, **2**(1), 129–136.

17 J.-G. Leu, S.-A. Chen, H.-M. Chen, W.-M. Wu, C.-F. Hung, Y.-D. Yao, C.-S. Tu and Y.-J. Liang, The effects of gold nanoparticles in wound healing with antioxidant epigallocatechin gallate and alpha-lipoic acid, *Nanomedicine*, 2012, **8**(5), 767–775.

18 R. Raguvaran, B. K. Manuja, M. Chopra, R. Thakur, T. Anand, A. Kalia and A. Manuja, Sodium alginate and gum acacia hydrogels of ZnO nanoparticles show wound healing effect on fibroblast cells, *Int. J. Biol. Macromol.*, 2017, **96**, 185–191.

19 S. Rose, A. Prevoteau, P. Elziere, D. Hourdet, A. Marcellan and L. Leibler, Nanoparticle solutions as adhesives for gels and biological tissues, *Nature*, 2014, **505**(7483), 382–385.

20 H. B. Wu, F. Y. Li, S. F. Wang, J. X. Lu, J. Q. Li, Y. Du, X. L. Sun, X. Y. Chen, J. Q. Gao and D. S. Ling, Ceria nanocrystals decorated mesoporous silica nanoparticle based ROS-scavenging tissue adhesive for highly efficient regenerative wound healing, *Biomaterials*, 2018, **151**, 66–77.

21 A. Meddahi-Pelle, A. Legrand, A. Marcellan, L. Louedec, D. Letourneur and L. Leibler, Organ Repair, Hemostasis, and In Vivo Bonding of Medical Devices by Aqueous Solutions of Nanoparticles, *Angew. Chem., Int. Ed.*, 2014, **53**(25), 6369–6373.

22 E. P. Ivanova, V. K. Truong, J. Y. Wang, C. C. Berndt, R. T. Jones, I. I. Yusuf, I. Peake, H. W. Schmidt, C. Fluke and D. Barnes, *et al.*, Impact of Nanoscale Roughness of Titanium Thin Film Surfaces on Bacterial Retention, *Langmuir*, 2010, **26**(3), 1973–1982.

23 V. K. Truong, R. Lapovok, Y. S. Estrin, S. Rundell, J. Y. Wang, C. J. Fluke, R. J. Crawford and E. R. Ivanova, The influence of nano-scale surface roughness on bacterial adhesion to ultrafine-grained titanium, *Biomaterials*, 2010, **31**(13), 3674–3683.

24 H. Song, Y. A. Nor, M. Yu, Y. Yang, J. Zhang, H. Zhang, C. Xu, N. Mitter and C. Yu, Silica Nanopollens Enhance Adhesion for Long-Term Bacterial Inhibition, *J. Am. Chem. Soc.*, 2016, **138**(20), 6455–6462.

25 N. Liu, Y. Chang, Y. L. Feng, Y. Cheng, X. J. Sun, H. Jian, Y. Q. Feng, X. Li and H. Y. Zhang, {101}–{001} Surface Heterojunction-Enhanced Antibacterial Activity of Titanium Dioxide Nanocrystals Under Sunlight Irradiation, *ACS Appl. Mater. Interfaces*, 2017, **9**(7), 5907–5915.

26 W. W. He, H. K. Kim, W. G. Warner, D. Melka, J. H. Callahan and J. J. Yin, Photogenerated Charge Carriers and Reactive Oxygen Species in ZnO/Au Hybrid Nanostructures with Enhanced Photocatalytic and Antibacterial Activity, *J. Am. Chem. Soc.*, 2014, **136**(2), 750–757.

27 L. Tan, J. Li, X. M. Liu, Z. D. Cui, X. J. Yang, S. L. Zhu, Z. Y. Li, X. B. Yuan, Y. F. Zheng and K. W. K. Yeung, *et al.*, Rapid Biofilm Eradication on Bone Implants Using Red Phosphorus and Near-Infrared Light, *Adv. Mater.*, 2018, **30**(31), 1801808.

28 P. Babilas, R. Knobler, S. Hummel, C. Gottschaller, T. Maisch, M. Koller, M. Landthaler and R. M. Szeimies, Variable pulsed light is less painful than light-emitting diodes for topical photodynamic therapy of actinic keratosis: a prospective randomized controlled trial, *Br. J. Dermatol.*, 2007, **157**(1), 111–117.

29 C. Wei, W. Y. Lin, Z. Zainal, N. E. Williams, K. Zhu, A. P. Kruzic, R. L. Smith and K. Rajeshwar, Bactericidal activity of TiO_2 photocatalyst in aqueous-media – toward a solar-assisted water disinfection system, *Environ. Sci. Technol.*, 1994, **28**(5), 934–938.

30 Y. Chang, Y. L. Feng, Y. Cheng, R. X. Zheng, X. Q. Wu, H. Jian, D. W. Zhang, Z. H. Tang, Z. X. Wang and J. M. Hao, *et al.*, Anisotropic Plasmonic Metal Heterostructures as Theranostic Nanosystems for Near Infrared Light-Activated Fluorescence Amplification and Phototherapy, *Adv. Sci.*, 2019, **6**(11), 1900158.

31 S. Linic, U. Aslam, C. Boerigter and M. Morabito, Photochemical transformations on plasmonic metal nanoparticles, *Nat. Mater.*, 2015, **14**(6), 567–576.

32 Y. Feng, X. Ning, J. Wang, Z. Wen, F. Cao, Q. You, J. Zou, X. Zhou, T. Sun and J. Cao, *et al.*, Mace-Like Plasmonic Au-Pd Heterostructures Boost Near-Infrared Photoimmunotherapy, *Adv. Sci.*, 2023, e2204842.

33 T. U. Luu, S. C. Gott, B. W. K. Woo, M. P. Rao and W. F. Liu, Micro- and Nanopatterned Topographical Cues for Regulating Macrophage Cell Shape and Phenotype, *ACS Appl. Mater. Interfaces*, 2015, **7**(51), 28665–28672.

34 J. Li, J. Wen, B. Li, W. Li, W. Qiao, J. Shen, W. Jin, X. Jiang, K. W. K. Yeung and P. K. Chu, Valence State Manipulation of Cerium Oxide Nanoparticles on a Titanium Surface for Modulating Cell Fate and Bone Formation, *Adv. Sci.*, 2018, **5**(2), 1700678.

35 X. Xie and N. A. Melosh, Fabrication of sub-cell size ''spiky'' nanoparticles and their interfaces with biological cells, *J. Mater. Chem. B*, 2015, **3**(26), 5155–5160.

36 J. Qu, X. Zhao, Y. P. Liang, T. L. Zhang, P. X. Ma and B. L. Guo, Antibacterial adhesive injectable hydrogels with rapid self-healing, extensibility and compressibility as wound dressing for joints skin wound healing, *Biomaterials*, 2018, **183**, 185–199.

37 M. E. Mahmoud, M. E. Abouelanwar, S. Mahmoud and M. A. Salam, Doping starch-gelatin mixed hydrogels with magnetic spinel ferrite@biochar@molybdenum oxide as a highly efficient nanocomposite for removal of lead(II) ions, *J. Environ. Chem. Eng.*, 2021, **9**(6), 106682.

38 N. A. Peppas, J. Z. Hilt, A. Khademhosseini and R. Langer, Hydrogels in biology and medicine: From molecular principles to bionanotechnology, *Adv. Mater.*, 2006, **18**(11), 1345–1360.

 This journal is © The Royal Society of Chemistry 2023

Open Access Article. Published on 25 2023. Downloaded on 30.5.2026 16:35:55.
This article is licensed under a Creative Commons Attribution-NonCommercial 3.0 Unported Licence.

39 E. Calo and V. V. Khutoryanskiy, Biomedical applications of hydrogels: A review of patents and commercial products, *Eur. Polym. J.*, 2015, **65**, 252–267.

40 Q. Xu, A. Sigen, Y. Gao, L. Guo, J. Creagh-Flynn, D. Zhou, U. Greiser, Y. Dong, F. Wang and H. Tai, *et al.*, A hybrid injectable hydrogel from hyperbranched PEG macromer as a stem cell delivery and retention platform for diabetic wound healing, *Acta Biomater.*, 2018, **75**, 63–74.

41 Y. P. Liang, J. H. He and B. L. Guo, Functional Hydrogels as Wound Dressing to Enhance Wound Healing, *ACS Nano*, 2021, **15**(8), 12687–12722.

42 Y. Dong, M. Rodrigues, S. H. Kwon, X. Li, A. Sigen, E. A. Brett, N. Elvassore, W. Wang and G. C. Gurtner, Acceleration of Diabetic Wound Regeneration using an *In Situ*-Formed Stem-Cell-Based Skin Substitute, *Adv. Healthcare Mater.*, 2018, **7**(17), 1800432.

43 N. R. Raia, B. Partlow, M. McGill, E. P. Kimmerling, C. E. Ghezzi and D. L. Kaplan, Enzymatically Crosslinked Silk-Hyaluronic Acid Hydrogels, *Tissue Eng., Part A*, 2016, **22**, S140–S140.

44 R. L. Zhao, H. L. N. Liang, E. Clarke, C. Jackson and M. L. Xue, Inflammation in Chronic Wounds, *Int. J. Mol. Sci.*, 2016, **17**(12), 2085.

45 N. X. Landen, D. Q. Li and M. Stahle, Transition from inflammation to proliferation: a critical step during wound healing, *Cell. Mol. Life Sci.*, 2016, **73**(20), 3861–3885.

46 S. Gordon and P. R. Taylor, Monocyte and macrophage heterogeneity, *Nat. Rev. Immunol.*, 2005, **5**(12), 953–964.

47 F. Liu, H. B. Qiu, M. Xue, S. Zhang, X. W. Zhang, J. Y. Xu, J. X. Chen, Y. Yang and J. F. Xie, MSC-secreted TGF-beta regulates lipopolysaccharide-stimulated macrophage M2-like polarization *via* the Akt/FoxO1 pathway, *Stem Cell Res. Ther.*, 2019, **10**(1), 345.